

One-Step Residual Shifting Diffusion for Image Super-Resolution via Distillation

Daniil Selikhanovych^{*1, 2, 4†} David Li^{*1, 3, 5} Aleksei Leonov^{*3, 5} Nikita Gushchin^{*1, 6}

Sergei Kushneriuk^{1, 2, 5} Alexander Filippov⁵ Evgeny Burnaev^{1, 6} Iaroslav Koshelev⁵

Alexander Korotin^{1, 6}

¹ Skoltech [‡] ² HSE University ³ MIPT[§] ⁴ Yandex Research
⁵ AI Foundation and Algorithm Lab ⁶ AIRI[¶]

Abstract

Diffusion models for super-resolution (SR) produce high-quality visual results but require expensive computational costs. Despite the development of several methods to accelerate diffusion-based SR models, some (e.g., SinSR) fail to produce realistic perceptual details, while others (e.g., OSediff) may hallucinate non-existent structures. To overcome these issues, we present **RSD**, a new distillation method for ResShift, one of the top diffusion-based SR models. Our method is based on training the student network to produce images such that a new fake ResShift model trained on them will coincide with the teacher model. RSD achieves single-step restoration and outperforms the teacher by a large margin. We show that our distillation method can surpass the other distillation-based method for ResShift - SinSR - making it on par with state-of-the-art diffusion-based SR distillation methods. Compared to SR methods based on pre-trained text-to-image models, RSD produces competitive perceptual quality, provides images with better alignment to degraded input images, and requires fewer parameters and GPU memory. We provide experimental results on various real-world and synthetic datasets, including RealSR, RealSet65, DRealSR, ImageNet, and DIV2K.

1 Introduction

Single image super-resolution (SR) [12, 16, 24] belongs to the category of inverse imaging problems aiming to reconstruct the high-resolution (HR) image given its low-resolution (LR) observation suffering from degradations. These degradations are usually *complex and unknown* for real-world scenarios when dealing with digital single-lens reflex cameras [3, 23, 62], referred to as the blind real-world image SR problem (Real-ISR). The SR problem is highly ill-posed, and many methods have been proposed in the literature to address it.

Recently, diffusion models have been developed for the blind SR problem [6, 7, 41, 43, 45, 56, 73] and became a strong alternative for methods based on generative adversarial networks (GAN) [25, 58, 74]

^{*}Equal contribution.

[†]Corresponding author: <selikhanovychdaniil@gmail.com>

[‡]Skolkovo Institute of Science and Technology

[§]Moscow Institute of Physics and Technology

[¶]Artificial Intelligence Research Institute

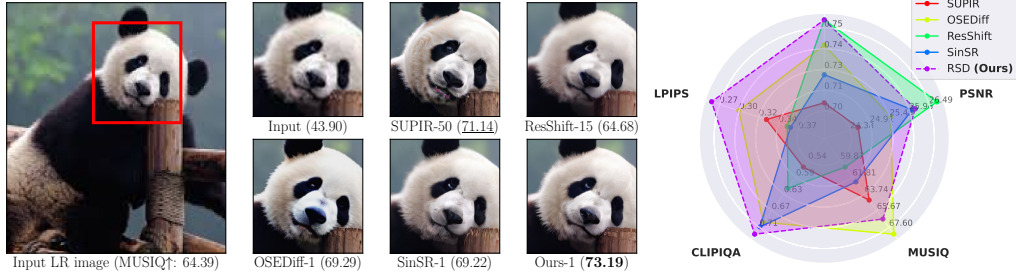


Figure 1: **Left.** A comparison between the recent diffusion-based methods for Real-ISR - ResShift [73], SinSR [59], OSEDiff [63], SUPIR [71] - and the proposed RSD method. Our model has two advantages compared with other distillation-based models: (1) It achieves superior perceptual quality compared to SinSR; (2) It requires less computational resources compared to OSEDiff; see Table 4. ("-N" behind the method name represents the number of inference steps, and the value in the bracket is MUSIQ↑ [26] for full images). Please zoom in $\times 5$ times for a better view. **Right.** Comparison among diffusion SR methods on RealSR [3]. RSD (**Ours**) achieves top scores on most metrics while remaining computationally efficient compared to T2I methods such as OSEDiff[63] and SUPIR[71].

due to their good capabilities to learn complex data distributions [10]. The competitive perceptual quality of diffusion models for different real-world SR problems is also supported by bigger human evaluation preferences compared to GAN-based methods, as shown in [45, 56]. Early diffusion methods for SR constructed a denoising process, which starts from Gaussian prior and ends in the HR image, while the LR image is used as a condition for the input of the denoiser [41, 43, 45].

However, this strategy also leads to significant computational resources and slow inference time, requiring dozens or hundreds for the number of function evaluations (NFE) of the denoiser and limiting diffusion models based on these strategies from practically important real-time SR on consumer devices. Consequent works for diffusion-based SR methods developed different approaches to accelerate those models while maintaining their high quality. Among them, ResShift [73] achieves perceptually high results in solving the Real-ISR problem using only 15 NFE. This model surpasses or provides competitive performance when compared with state-of-the-art (SOTA) models from the other classes, including GANs [25, 33, 58, 74], transformers [31] and previous diffusion models [43].

However, the inference time for ResShift still remains 10 times larger than that of GAN-based models, as shown in [73, Table 2]. The challenge arises when considering the problem of further acceleration of diffusion models while maintaining their perceptual quality at the same level. As shown in SinSR [59], ResShift exhibits degraded performance with artifacts if NFE is further reduced. To overcome this problem, SinSR [59] proposed a knowledge distillation algorithm for ResShift in 1 NFE, which is based on the deterministic sampling formulation of the reverse process for ResShift inspired by DDIM sampling [49]. But SinSR tends to produce not satisfactory perceptual results with blurriness, as can be seen in the first row of Figure 3 and was also pointed out in several recent works [14, 53, 63].

Another promising direction in acceleration of diffusion models for super-resolution is to add conditioning on the LR image to pre-trained text-to-image (T2I) models [42–44] with LoRA [21] and distill them with variational score distillation [8, 61, 70] as proposed by OSEDiff [63]. While this approach greatly reduced NFE from tens or even hundreds to one across the class of T2I-based SR models [35, 56, 64, 68, 71] and achieved better perceptual results than ResShift and SinSR, we observe the following issues with T2I-based models for the SR problem: (1) as we show Table 4, using computationally expensive T2I architectures like Stable Diffusion [42, 43] still leads to high computational cost and requires $\times 10$ more parameters than SinSR; (2) T2I-based models for SR also produce lower full-reference fidelity metrics such as PSNR and SSIM [60] when compared with ResShift and SinSR, as shown for various synthetic and real-world SR benchmarks in Table 2 and Table 3, aligning with [53, 63].

Due to these issues of distillation methods for diffusion SR, we address the following **3 questions**.

1. Are knowledge distillation and variational score distillation the best candidates for achieving efficient 1-step diffusion SR?

2. Can we unite the *best of two worlds* for those distillation methods and achieve a 1-step diffusion-based SR model that has a good perceptual quality comparable to SOTA T2I-based diffusion SR models like OSEDiff and good fidelity preservation like SinSR at the same time?
3. Can we achieve this goal and avoid computationally demanding T2I models, bringing diffusion models closer to being deployed in practical SR scenarios with a limited computational budget?

Contributions. Our main contributions are as follows:

(I) Theory. Inspired by the successful distillation of ResShift achieved by SinSR and recent progress in the distillation of image-to-image diffusion models [19], we propose a novel objective for the 1-step distillation of the diffusion-based SR model and derive its tractable version. Motivated by ResShift’s superior perception-distortion trade-off across SOTA diffusion-based models and its mathematically justified diffusion process, we build our method on top of it and name our method as **RSD: Residual Shifting Distillation**.

(II) Practice. We show that our models trained with the proposed objective combined with additional supervised losses notably surpass the teacher’s results on the real-world SR problem for various perceptual metrics, including LPIPS [77], CLIPQA [54], and MUSIQ [26]. Our method aims to improve the compromise between fidelity, perceptual quality, and computational efficiency for diffusion real-world SR models in several aspects, see Figure 1 and Table 4:

1. **Perceptual quality.** Compared to the other 1-step distillation-based method for ResShift - SinSR - our method achieves better perceptual quality on synthetic and real-world benchmarks for the blind SR problem.
2. **Fidelity quality.** Compared to the other 1-step diffusion SR model, which is based on pre-trained T2I models - OSEDiff - our method provides competitive perceptual results or even surpasses it while having better fidelity.
3. **Computational efficiency.** Similarly to SinSR, to bring diffusion models closer to real-time SR applications, our method suggests an alternative algorithm for the 1-step distillation of ResShift model, leading to lower computational budget compared to T2I-based SR models.

2 Related work

GAN-based SR models. With the rise of GAN perspective [17], one line of research adapted the GAN framework to the SR problem [28, 46, 58, 74] and achieved much better perceptual quality of the generated HR images than previously developed regression-based methods [12, 13, 27, 34, 78], which minimize the mean squared error (MSE) between the recovered HR image and the ground truth. Among those works, Real-ESRGAN [58] and BSRGAN [74] suggested effective degradation pipelines to synthesize explicitly LR-HR image pairs for modeling real-world data. Previous methods assumed a pre-defined degradation process (e.g., bicubic), which leads to limited generalizability. The degradation pipelines of [58, 74] improved the results of GAN-based SR models for real-world images and have also been widely used by diffusion [56, 63, 73] and transformer SR models [31].

Diffusion-based SR models. Existing methods, which adapt diffusion models [20, 48, 50, 51] for the blind SR problem, can be split into several categories depending on how they utilize the LR image. The first category of methods uses the LR image as an additional condition for the input of the denoiser and trains the denoiser from scratch [41, 43, 45]. The second category of methods utilizes unconditional to the LR image pre-trained diffusion priors and modifies the reverse process of diffusion models [6, 7, 56]. The third category of diffusion-based SR methods argues that large NFE is needed for those models due to the Gaussian prior, which is not optimal for an SR problem where the LR image already contains structural information about the HR image. Following this motivation, methods from the third category suggest starting the denoising process from the combination of the LR image and a random noise while solving the blind SR problem [36, 72, 73]. As a representative SR model from this class, ResShift [73] has several advantages: **(1)** it achieves SOTA results for blind *real-world* SR using only 15 NFE; at the same time methods [36, 72] considered only simple degradations and used hundreds of NFE; **(2)** similar to LDM [43], ResShift performs a diffusion process in the latent space of an autoencoder [15], and is also 2-4 times faster and provides better perception-distortion trade-off than LDM.

Acceleration of diffusion-based SR models. While diffusion models surpass GANs in generative performance [10], their slow inference remains the key challenge. To mitigate this issue, various acceleration techniques have been proposed, with distillation emerging as one of the most effective approaches. These methods have also been extended to diffusion-based SR models. For instance, to further improve the efficiency of ResShift, SinSR [59] applied knowledge distillation [39] to its diffusion process. By introducing a consistency-preserving loss that uses ground-truth data during training, SinSR achieved performance comparable to or better than the teacher ResShift model for blind real-world SR while requiring only 1 NFE. In our work, we draw inspiration from distillation techniques that involve training an auxiliary "fake" model [18, 22, 40, 69, 80]. We give a detailed discussion of relation of our work method to these approaches in Appendix A.

T2I-based SR models. However, as pointed out in several recent works [14, 63, 64], ResShift and SinSR show lower perceptual quality metrics and may fail to synthesize realistic structures when compared with other diffusion-based methods, which exploit pre-trained T2I diffusion models for blind real-world SR problem. The possible reason for this is the limited generalization of ResShift and SinSR, which is constrained due to the absence of large-scale data for the training. On the contrary, T2I models [42–44] were trained on billions of image-text pairs and became the natural choice for applying to real-world SR. To adapt T2I models for SR problem, such methods usually have two components: (1) conditioning on the LR image is realized with T2I controllers such as LoRA layers [21] (OSDiff [63]), ControlNet approach [76] (SeeSR [64], DiffBIR [35], SUPIR [71]) or other modules (StableSR [56], PASD [68]); (2) prompts for LR images are used as predefined (StableSR [56], DiffBIR [35]) or extracted with additional models such as DAPE [64] (SeeSR [64], OSDiff [63]), LLaVA [37] (SUPIR [71]), or BLIP [29] (PASD [68]).

However, such adaptations to image restoration also lead to different challenges. The first challenge is their computationally demanding requirements, as many methods utilizing pre-trained T2I models for real-world SR require tens or even hundreds of NFE [35, 56, 64, 68, 71]. The recently developed one-step diffusion distillation methods utilize different ideas, including variational score distillation (VSD) [8, 61, 70] (OSDiff [63]), adversarial diffusion distillation [47] (AddSR [65]), or target score distillation (TSD-SR [14]). These methods significantly reduce the inference time of T2I-based SR models but do not solve the problem of inheritance of costly demanded T2I architectures with billion parameters. The second challenge of those models is their unstable predictions for the fixed input due to high dependence on noise initialization for the start of the denoising process, as pointed out in CCSR [53]. Such instability may lead to poor fidelity and random unfaithful details.

3 Method

We start by recalling the ResShift formulation in §3.1. Then, we propose our method for distillation of the ResShift teacher model in a one-step generator and derive its computationally tractable form in §3.2. We expand the method to the multistep generator in §3.3 and add additional supervised losses in §3.4. We then combine everything and formulate the total objective for our RSD method in §3.5.

Remark. While we derive our distillation method RSD for ResShift, we note that ResShift is essentially a conditional DDPM [20] diffusion, where the forward process ends in a Gaussian centered at the LR image. Therefore, our distillation method can be generalized, if needed, to any diffusion model built on the DDPM framework.

3.1 Background

As a part of the diffusion model class, ResShift can be described by specifying the forward (noising) process, the parametrization of the reverse (denoising) process, and the objective for training the reverse process.

Forward process. Consider a pair of (LR, HR) images $(y_0, x_0) \sim p_{\text{data}}(y_0, x_0)$. For a residual $e_0 = y_0 - x_0$, ResShift uses the forward process with Gaussian kernel:

$$q(x_t | x_{t-1}, y_0) = \mathcal{N}(x_t | x_{t-1} + \alpha_t e_0, \kappa^2 \alpha_t \mathbf{I}), \quad (1)$$

where $\alpha_t = \eta_t - \eta_{t-1}$, $\alpha_1 = \eta_1$ and $\{\eta\}_{t=1}^T$ is a schedule, while k is a hyper-parameter controlling the noise variance. The corresponding posterior distribution is given as:

$$q(x_{t-1} | x_t, x_0, y_0) = \mathcal{N}\left(x_{t-1} \middle| \frac{\eta_{t-1}}{\eta_t} x_t + \frac{\alpha_t}{\eta_t} x_0, \frac{\kappa^2 \eta_{t-1}}{\eta_t} \alpha_t \mathbf{I}\right) \quad (2)$$

Reverse process. ResShift suggests the reverse process in the following parametrized form:

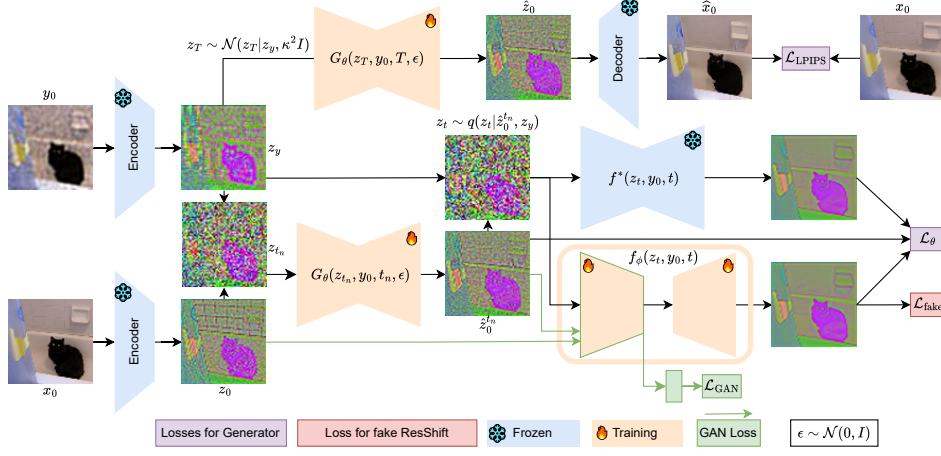


Figure 2: **The training framework of RSD.** We begin by encoding the (LR, HR) pair (y_0, x_0) into the latent space (z_y, z_0) . First, to compute the LPIPS loss $\mathcal{L}_{\text{LPIPS}}$, we use z_y to sample z_T and generate the output \hat{z}_0 from timestep T (following procedure of one-step inference), then decode it back to pixel space to obtain \hat{x}_0 . Second, for the multistep distillation loss, we obtain input data z_{t_n} from the forward diffusion process in latent space (1) and generate $\hat{z}_0^{t_n}$. We then perform posterior sampling (2) to obtain z_t , process it using both the fake and teacher ResShift models, and compute the distillation losses \mathcal{L}_θ and $\mathcal{L}_{\text{fake}}$ from Proposition 3.1. Finally, to compute the GAN loss \mathcal{L}_{GAN} , we extract features from the encoder part of the fake model f_ϕ and use an additional discriminator head.

$$p_\theta(x_0|y_0) = \int p(x_T|y_0) \prod_{t=1}^T p_\theta(x_{t-1}|x_t, y_0) dx_{1:T} \quad (3)$$

Here $p(x_T|y_0) = \mathcal{N}(x_T|y_0, \kappa^2 I)$, and $p_\theta(x_{t-1}|x_t, y_0)$ is the reverse transition kernel from x_{t-1} to x_t approximated with Gaussian distribution with parameters μ_θ and Σ_θ .

Objective. ResShift sets the variance parameter $\Sigma_\theta(x_t, y_0, t)$ to be independent of x_t and y_0 and reparametrizes the parameter $\mu_\theta(x_t, y_0, t)$ as:

$$\mu_\theta(x_t, y_0, t) = \frac{\eta_{t-1}}{\eta_t} x_t + \frac{\alpha_t}{\eta_t} f_\theta(x_t, y_0, t), \quad (4)$$

where f_θ is a deep neural network with parameter θ , aiming to predict x_0 . The training objective is:

$$\min_{\theta} \left[\sum_{t=1}^T \mathbb{E}_{p(x_0, y_0, x_t)} w_t \|f_\theta(x_t, y_0, t) - x_0\|^2 \right], \quad (5)$$

where w_t are some positive weights and $p(x_0, y_0, x_t)$ is provided by the forward process of ResShift. More detailed information on ResShift can be found in Appendix E.

3.2 Residual Shifting Distillation (RSD)

Our goal is to distill a given ResShift *teacher* model $f^*(x_t, y_0, t)$ into a stochastic one-step *student* generator G_θ , which maps the LR image y_0 to the HR image x_0 . To achieve this goal, we parametrize the generator $\hat{x}_0 = G_\theta(x_T, y_0, \epsilon)$ to have three inputs: the LR image y_0 , its noisy version $x_T \sim q(x_T|y_0)$ and additional noise input $\epsilon \sim \mathcal{N}(\epsilon|0, I)$. We denote by $p_\theta(\hat{x}_0|x_T, y_0)$ the distribution of G_θ produced for given y_0, x_T and random ϵ . Then, **we force the generator to produce such data $p_\theta(\hat{x}_0|y_0)$, that ResShift trained on it will coincide with the teacher model $f^*(x_t, y_0, t)$.** We consider the following minimization problem:

$$\min_{\theta} \mathcal{L}_\theta, \quad \text{where} \quad \mathcal{L}_\theta \stackrel{\text{def}}{=} \sum_{t=1}^T w_t \mathbb{E}_{p_\theta(\hat{x}_0, y_0, x_t)} \|f_{G_\theta}(x_t, y_0, t) - f^*(x_t, y_0, t)\|_2^2 \quad (6)$$

and $p_\theta(\hat{x}_0, y_0, x_t)$ is provided by mapping LR image by a generator $\hat{x}_0 = G_\theta(x_T, y_0, \epsilon)$ and using posterior distribution $q(x_t|\hat{x}_0, y_0)$ given in (2). In turn, $f_{G_\theta}(x_t, y_0, t)$ is the ResShift model trained on the generator data $p_\theta(\hat{x}_0|y_0)$. The gradient $\nabla_\theta \mathcal{L}_\theta$ includes the term $\nabla_\theta f_{G_\theta}(x_t, y_0, t)$, which is not tractable since the backpropagation through the whole learning of the ResShift model $f_{G_\theta}(x_t, y_0, t)$ is computationally infeasible. To solve the problem, we propose another equivalent expression of \mathcal{L}_θ :

Proposition 3.1. *For a given teacher model $f^*(x_t, y_0, t)$, loss in (6) can be evaluated in a tractable form as:*

$$\mathcal{L}_\theta = -\min_{\phi} \left\{ \sum_{t=1}^T w_t \mathbb{E}_{p_\theta(\hat{x}_0, y_0, x_t)} \left(-\|f^*(x_t, y_0, t)\|_2^2 + \underbrace{\|f_\phi(x_t, y_0, t)\|_2^2 - 2\langle f_\phi(x_t, y_0, t) - f^*(x_t, y_0, t), \hat{x}_0 \rangle}_{\text{This objective } \mathcal{L}_{\text{fake}} \text{ is equivalent to training a fake model } f_\phi \text{ with objective (5)}} \right) \right\}. \quad (7)$$

Here, f_ϕ represents an additional ResShift model trained to optimize objective $\mathcal{L}_{\text{fake}}$ in (7) in order to estimate \mathcal{L}_θ . Furthermore, minimizing (7) over ϕ is equivalent to training a "fake" ResShift model using data generated by G_θ .

Thus, we alleviate the original problem of the intractable gradient in (6) by incorporating the loss of training of the fake ResShift model into objective \mathcal{L}_θ (6). We provide the proof of Proposition 3.1 in Appendix G. For completeness, in Appendix A.1, we also compare our method with another method involving fake models [70] used in OSDiff [63].

3.3 Multistep RSD training

To further improve the quality of images produced by our method, we consider the multistep training of the generator following previous diffusion distillation works [52, 69, 80]. We fix a subset of N timesteps $1 < t_1 < \dots < t_N = T$ and append additional time conditioning for the generator $G_\theta(x_t, t, y_0, \epsilon)$. We denote by $\hat{x}_0^{t_n}$ output of generator $G_\theta(x_t, t, y_0, \epsilon)$ at timestep t_n . In this setup, the generator G_θ should approximate distributions $p_\theta(\hat{x}_0|x_{t_n}, y_0) \approx q(x_0|x_{t_n}, y_0)$ for all fixed timesteps t_n instead of only approximating the distribution $p_\theta(\hat{x}_0|x_T, y_0) \approx q(x_0|x_T, y_0)$ in one-step training. For multistep training, we generate input data $q(x_{t_n}|y_0)$ using ground truth data distribution $p(x_0|y_0)$ of LR and HR images and posterior distribution (2). Then, we use the objective from Proposition 3.1 to train the generator for all t_n simultaneously. At inference, we use a single sampling step to maximize speed. This strategy shows better results than one-step training since training across multiple time steps appears to help the network learn more robust mappings (see Table 5). For consistency, we denote the output of the single-step network at the timestep T by \hat{x}_0 .

3.4 Supervised losses

In our distillation approach, we rely on the teacher's prediction to guide the solution. However, this approach may yield suboptimal results due to inherent approximation errors in the estimation of x_0 . To mitigate this issue, we integrate additional losses into the distillation process.

LPIPS loss. Inspired by OSDiff [63], we used LPIPS loss in our approach. By employing LPIPS loss ($\mathcal{L}_{\text{LPIPS}}$ [77]), we enable the student model to directly compare its output with the high-resolution ground truth in terms of perceptual features. This comparison helps the network to recover essential textures and structural details that might be missed when relying on the teacher's guidance. Although OSDiff also used MSE loss for better fidelity alignment, we found that it did not help in our setup.

GAN loss. In line with DMD2 [69], we integrate a GAN loss into our framework. Incorporating the GAN loss enhances the student model's capacity to align its predictions with the distribution of high-resolution images, thereby yielding overall superior image quality. Our minimalist design - adding a classification branch to the bottleneck of the fake ResShift (see Figure 2) - mirrors DMD2. While previous works [66, 69] implemented GAN loss for comparing marginal distributions of noised data and generator output, we notice that using GAN loss to compare clean data distribution $p_{\text{data}}(x_0|y_0)$ with clean generator distribution $p_\theta(\hat{x}_0^{t_n}|y_0)$ at each timestep t_n is more effective:

$$\mathcal{L}_{\text{GAN}} = \mathbb{E}_{p_{\text{data}}(x_0|y_0)} [\log D(x_0|y_0)] - \mathbb{E}_{p_\theta(\hat{x}_0^{t_n}|y_0)} [\log D(\hat{x}_0^{t_n}|y_0)]. \quad (8)$$

3.5 Putting everything together

Translation into a latent space. Thus far, we assumed that loss functions operate in the image space (denoted as x), although the ResShift model was originally trained in the latent space (denoted as z). We also move our losses to the latent space, eliminating redundant latent encoding and decoding when computing losses. Specifically, we calculate the distillation loss (\mathcal{L}_θ) and GAN loss (\mathcal{L}_{GAN}) in the latent space, while the LPIPS loss ($\mathcal{L}_{\text{LPIPS}}$) remains in the image space, as the LPIPS network was originally trained there.

Final algorithm. The final loss function for each t_n is:

$$\mathcal{L}_\theta + \lambda_1 \mathcal{L}_{\text{LPIPS}} + \lambda_2 \mathcal{L}_{\text{GAN}} \quad (9)$$

A detailed description of the complete algorithm is provided in Appendix B, with a corresponding illustration in Figure 2.

4 Experiments

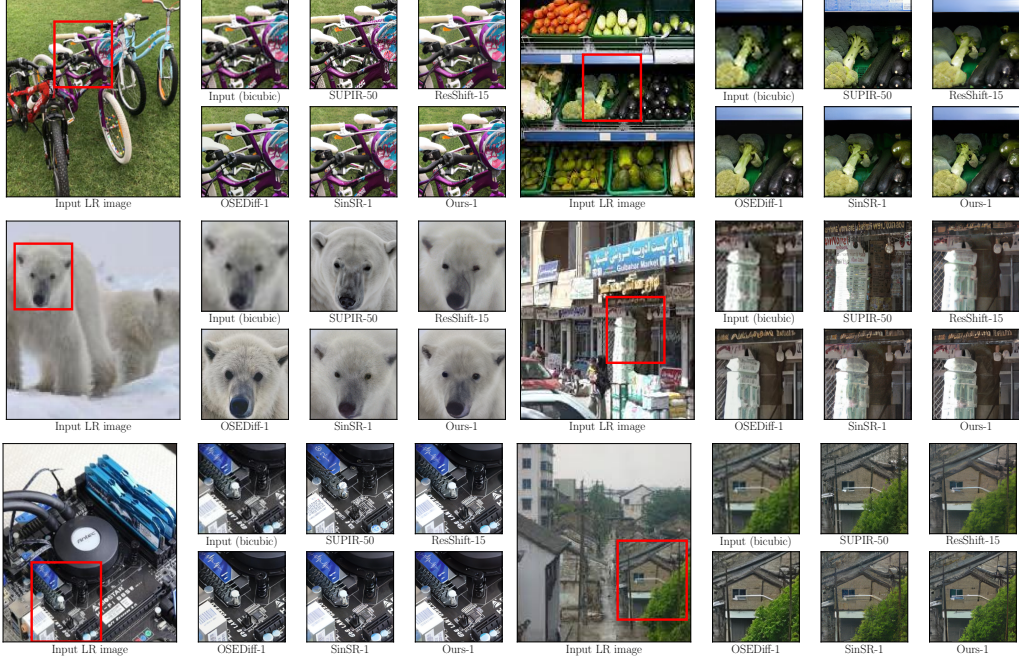


Figure 3: Visual comparison on Real-ISR from RealSet65 [73]. Please zoom in $\times 5$ times for a better view.

In this section, we aim to achieve two main objectives: **(1)** to demonstrate that our proposed *distillation* method outperforms existing *distillation* methods under the same experimental setup. We chose the setup of ResShift [73] to be consistent with our teacher model and SinSR [59]. We show our enhancements compared to the current best SOTA ResShift distillation method known as SinSR, and for comprehensive evaluation of our distillation method, we also implement OSEDiff VSD-based method applied to ResShift setup, called **ResShift-VSD** (see Appendix A.1); **(2)** to show that RSD achieves perceptual performance competitive with SOTA T2I-based SR methods such as OSEDiff [63] and SUPIR [71] while maintaining a smaller architecture and better fidelity. These objectives are supported by evaluations using the experimental setups employed in SinSR and OSEDiff. We present two types of models: RSD (**Ours**, distill only), where we used only distillation \mathcal{L}_θ loss during training, and RSD (**Ours**), where we use distillation combined with additional losses (§3.4). Appendix C provides all relevant experiment details.

4.1 Experimental setup

Training and evaluation details. For a fair comparison, we follow the *training setup* of SinSR and ResShift, using 256×256 HR images randomly cropped from ImageNet [9] and generating LR images via the Real-ESRGAN [58] degradation pipeline with $\times 4$ SR factor. We also adopt the ResShift teacher model used in SinSR. *For the evaluation*, we follow two different protocols from SinSR and OSEDiff ($\times 4$ SR factor). Following SinSR, we use the following datasets: (1) for real-world degradations, we use full-size images from RealSR [3] and RealSet65 [73]; (2) for synthetic degradations, we use ImageNet-Test [73]. Following OSEDiff, we use test sets of HR crops 512×512 from StableSR [56], including synthetic DIV2K-Val [1] and real-world pairs from RealSR and DRealSR [62].

Compared methods. Our study follows two distinct experimental setups with different baseline comparisons. Following [59, Table 1 and Table 2], we incorporate several baselines from SinSR evaluation setups for real-world and synthetic datasets. In the main text, we compare our method against **diffusion-based** SR models: ResShift, SinSR, and additionally recent SOTA T2I-based SR models - one-step OSEDiff [63] and multistep SUPIR [71]. In Appendix D, we provide quantitative results of other baselines, including GAN-based models [25, 57, 58, 74], SwinIR [31], LDM [43], and

Table 1: Quantitative results of models on two real-world datasets. The best and second best results are highlighted in **bold** and underline.

Methods	NFE	Datasets						
		<i>RealSR</i>					<i>RealSet65</i>	
		PSNR \uparrow	SSIM \uparrow	LPIPS \downarrow	CLIPQA \uparrow	MUSIQ \uparrow	CLIPQA \uparrow	MUSIQ \uparrow
SUPIR [71]	50	24.38	0.698	0.331	0.5449	63.676	0.6133	66.460
OSDiff [63]	1	25.25	0.737	0.299	0.6772	67.602	0.6836	<u>68.853</u>
ResShift [73]	15	26.49	0.754	0.360	0.5958	59.873	0.6537	61.330
SinSR (distill only) [59]	1	<u>26.14</u>	0.732	0.357	0.6119	57.118	0.6822	61.267
SinSR [59]	1	25.83	0.717	0.365	0.6887	61.582	0.7150	62.169
ResShift-VSD (Appendix A.1)	1	23.96	0.616	0.466	<u>0.7479</u>	63.298	0.7606	66.701
RSD (Ours, distill only)	1	24.92	0.696	0.355	0.7518	<u>66.430</u>	<u>0.7534</u>	68.383
RSD (Ours)	1	25.91	<u>0.754</u>	0.273	0.7060	65.860	0.7267	69.172

Table 2: Quantitative results of models on ImageNet-Test [73]. The best and second best results are highlighted in **bold** and underline.

Methods	NFE	PSNR \uparrow	SSIM \uparrow	LPIPS \downarrow	CLIPQA \uparrow	MUSIQ \uparrow
SUPIR [71]	50	22.56	0.574	0.302	0.786	<u>60.487</u>
OSDiff [63]	1	23.02	0.619	0.253	0.677	60.755
ResShift [73]	15	25.01	0.677	0.231	0.592	53.660
SinSR (distill only) [59]	1	<u>24.69</u>	<u>0.664</u>	0.222	0.607	53.316
SinSR [59]	1	24.56	0.657	0.221	0.611	53.357
ResShift-VSD (Appendix A.1)	1	23.69	0.624	0.230	0.665	58.630
RSD (Ours, distill only)	1	23.97	0.643	<u>0.217</u>	0.660	57.831
RSD (Ours)	1	24.31	0.657	0.193	<u>0.681</u>	58.947

DASR [33]. For the **OSDiff** evaluation setup, we compared our method in the main text against **diffusion-based** SR models, including ResShift, SinSR, OSDiff, and SUPIR. We also compare RSD with other baselines in Appendix D, including multistep T2I-based [35, 56, 64, 68] and GAN-based SR methods [5, 32, 58, 74].

Metrics. Each setup employs different evaluation metrics, which we adopt from SinSR [59, Table 1 and Table 2] and **OSDiff** [63, Table 1]. For all evaluation setups from SinSR, we compute image-quality no-reference metrics CLIPQA [55] and MUSIQ [26] following SinSR. In the **OSDiff** configuration, evaluation is conducted using fidelity metrics, including PSNR and SSIM, full-reference perceptual metrics, including LPIPS and DISTs [11], and no-reference image-quality metrics, including NIQE [75], MANIQA-PIPAL [67], MUSIQ, and CLIPQA. We calculate PSNR and SSIM on the Y channel of the YCbCr space following SinSR and **OSDiff**.

4.2 Experimental results

Quantitative comparisons. The key quantitative results are summarized in Table 1, Table 2, Table 3 and visualized in Figure 1. We make the following observations based on them. (1) Our model outperforms the teacher ResShift model and our closest competitor, SinSR, by a large margin for all **perceptual** metrics (LPIPS, CLIPQA, MUSIQ, DISTs, NIQE, MANIQA) and **all test datasets** while training on the same data. At the same time, it also has competitive fidelity metrics such as PSNR and SSIM. Furthermore, RSD demonstrates comparable or even better results than the implemented OSDiff distillation method for the ResShift model, ResShift-VSD (Appendix A.1). (2) Compared to T2I-based OSDiff and SUPIR models on real-world benchmarks, our model achieves the best value of the latest image-quality CLIPQA and top-1 or top-2 results in terms of MUSIQ. Our model achieves worse CLIPQA than SUPIR for synthetic datasets but better than OSDiff. We hypothesize the gap with SUPIR is due to its multistep nature, rich SDXL prior [42], and large proprietary dataset with high-quality images, which leads to better details and better preferences by no-reference metrics. However, this also leads to poor consistency with the LR image, as noticeable by PSNR, SSIM, and LPIPS metrics. We highlight that our model, even with slightly worse MUSIQ, achieves much better fidelity metrics than OSDiff and SUPIR for most setups while utilizing a much

Table 3: Quantitative results of models on crops 512×512 from [56]. The best and second best results are highlighted in **bold** and underline.

Datasets	Methods	NFE	PSNR \uparrow	SSIM \uparrow	LPIPS \downarrow	DISTS \downarrow	NIQE \downarrow	MUSIQ \uparrow	MANIQA \uparrow	CLIPQA \uparrow
DIV2K-Val	SUPIR [71]	50	22.13	0.5280	0.3923	0.2314	5.6758	63.82	0.5933	0.7147
	ResShift [73]	15	24.65	0.6181	0.3349	0.2213	6.8212	61.09	0.5454	0.6071
	SinSR [59]	1	<u>24.41</u>	0.6018	0.3240	0.2066	6.0159	62.82	0.5386	0.6471
	OSDiff [63]	1	23.72	<u>0.6108</u>	<u>0.2941</u>	<u>0.1976</u>	4.7097	<u>67.97</u>	0.6148	0.6683
	RSD (Ours)	1	23.91	0.6042	0.2857	0.1940	<u>5.1987</u>	68.05	<u>0.5937</u>	<u>0.6967</u>
DrealSR	SUPIR [71]	50	24.93	0.6360	0.4263	0.2823	7.4336	59.39	0.5537	0.6799
	ResShift [73]	15	28.46	<u>0.7673</u>	0.4006	0.2656	8.1249	50.60	0.4586	0.5342
	SinSR [59]	1	<u>28.36</u>	0.7515	0.3665	0.2485	6.9907	55.33	0.4884	0.6383
	OSDiff [63]	1	27.92	0.7835	0.2968	0.2165	<u>6.4902</u>	64.65	0.5899	<u>0.6963</u>
	RSD (Ours)	1	27.40	0.7559	<u>0.3042</u>	<u>0.2343</u>	6.2577	<u>62.03</u>	<u>0.5625</u>	0.7019
RealSR	SUPIR [71]	50	23.61	0.6606	0.3589	0.2492	5.8877	63.21	0.5895	0.6709
	ResShift [73]	15	26.31	0.7421	0.3421	0.2498	7.2365	58.43	0.5285	0.5442
	SinSR [59]	1	<u>26.28</u>	0.7347	0.3188	0.2353	6.2872	60.80	0.5385	0.6122
	OSDiff [63]	1	25.15	0.7341	<u>0.2921</u>	0.2128	5.6476	69.09	0.6326	<u>0.6693</u>
	RSD (Ours)	1	25.61	<u>0.7420</u>	0.2675	<u>0.2205</u>	<u>5.7500</u>	<u>66.02</u>	<u>0.5930</u>	0.6793

smaller number of parameters and GPU memory, as shown in Table 4. (3) In Table 3, we show that our model achieves top-2 or top-1 perceptual reference (LPIPS, DISTS) and no-reference (NIQE, MUSIQ, MANIQA, CLIPQA) metrics across all compared diffusion models. For some perceptual metrics, OSDiff sometimes achieves better values. However, we highlight the different training HR resolution of RSD with OSDiff - we used HR crops of the size 256×256 as in the teacher ResShift model, while OSDiff used HR crops of the size 512×512 for training on LSDIR [30], which aligns with crop size in Table 3. This discrepancy in training resolutions indicates that the evaluation setup is more suited to OSDiff, introducing a potential bias in favor of OSDiff that should be considered when interpreting the results. Additional quantitative results are presented in Appendix D.

Qualitative comparisons. We visually compare our method with SinSR, OSDiff, ResShift, and SUPIR on several test images from RealSet65 in Figure 3. As illustrated in the top two images - bicycle and vegetables - SUPIR tends to produce rich details that semantically don't correspond to the LR image. Please zoom in for excessive lines and broccolis, respectively. ResShift and SinSR produce more conservative images, which may struggle from severely blurred details like the house's roof on the bottom right image. OSDiff also sometimes hallucinates excessive details, as can be seen for the bear's nose in Figur 3 and panda's nose in Figure 1. Our method compromises between the good details of OSDiff and SUPIR and the high fidelity of ResShift and SinSR. Additional visual results are presented in Appendix H.

Complexity comparisons. We compare the complexity of competing diffusion-based SR models in Table 4, including the number of inference steps, inference time, total number of parameters, and maximum required GPU memory during inference. All methods are tested on an NVIDIA A100 GPU with an HR image of size 256×256 following the training setup of ResShift, SinSR and RSD. We observe that RSD and SinSR require at least $\times 5$ less GPU memory and have $\times 10$ fewer parameters than T2I-based models, which highlights the efficiency of those models in terms of computational budget and can be useful for consumer devices.

Table 4: Complexity comparison among different methods. All methods are tested with an input LR image of size 64×64 for scale factor $\times 4$, and the inference time is measured on an NVIDIA A100 GPU. The best values are highlighted in **bold**.

Methods	ResShift [73]	SinSR [59]	SUPIR [71]	OSDiff [63]	RSD (Ours)
Inference Step	15	1	50	1	1
Inference Time (s)	0.643	0.060	17.704	0.075	0.059
# Total Param (M)	174	174	4801	1775	174
Maximum GPU memory (MB)	1167	570	52535	3651	539

4.3 Ablation study

Multistep training. We analyze the performance of our method under different timestep configurations in multistep training §3.3. As shown in Table 5, we compare various numbers of timesteps N ranging from 1 to 15 with the maximum number matching that of ResShift; timesteps are evenly placed. Selecting $N = 4$ provides the optimal choice for the compromise between perceptual quality and distortion, which is known as perceptual-distortion trade-off [2].

Table 5: Impact of multistep training of our RSD on RealSR [3]. The best and second best results are highlighted in **bold** and underline.

N	PSNR \uparrow	LPIPS \downarrow	CLIPQA \uparrow	MUSIQ \uparrow
1	24.82	0.4052	0.7444	64.290
2	24.77	0.3772	0.7523	65.760
4	24.92	0.3552	<u>0.7518</u>	<u>66.430</u>
8	<u>25.63</u>	<u>0.3199</u>	0.7286	66.445
15	25.91	0.2940	0.6857	65.689

Table 6: Effect of incorporating supervised losses on RealSR [3]. The best and second best results are highlighted in **bold** and underline.

Method	PSNR \uparrow	LPIPS \downarrow	CLIPQA \uparrow	MUSIQ \uparrow
$\lambda_{1,2} = 0$	24.92	0.3552	0.7518	<u>66.430</u>
$\lambda_1 \neq 0$	26.01	0.2708	<u>0.7089</u>	65.178
$\lambda_2 \neq 0$	24.98	0.3064	0.6970	67.615
Ours	<u>25.91</u>	<u>0.2726</u>	0.7060	65.860

Supervised losses. Table 6 examines the impact of incorporating supervised losses, as discussed in §3.4. Our results show that adding these losses significantly enhances quality in PSNR, SSIM and in LPIPS while introducing compromised yet acceptable changes in no-reference metrics (CLIPQA, MUSIQ). In all evaluations, we use full-size images with real-world degradations from RealSR.

5 Conclusion and future work

In this work, we propose RSD, a novel approach to distill the ResShift model into a student network with a single inference step. Our model is computationally efficient thanks to its ResShift framework but remains constrained by its teacher model. A more advanced teacher, such as a T2I-based model, could improve performance and enable the application of our method at higher resolutions.

References

- [1] Eirikur Agustsson and Radu Timofte. Ntire 2017 challenge on single image super-resolution: Dataset and study. In *Proceedings of the IEEE conference on computer vision and pattern recognition workshops*, pages 126–135, 2017.
- [2] Yochai Blau and Tomer Michaeli. The perception-distortion tradeoff. In *2018 IEEE/CVF Conference on Computer Vision and Pattern Recognition*, pages 6228–6237, 2018.
- [3] Jianrui Cai, Hui Zeng, Hongwei Yong, Zisheng Cao, and Lei Zhang. Toward real-world single image super-resolution: A new benchmark and a new model. In *2019 IEEE/CVF International Conference on Computer Vision (ICCV)*, pages 3086–3095, 2019.
- [4] Chaofeng Chen and Jiadi Mo. IQA-PyTorch: Pytorch toolbox for image quality assessment. [Online]. Available: <https://github.com/chaofengc/IQA-PyTorch>, 2022.
- [5] Chaofeng Chen, Xinyu Shi, Yipeng Qin, Xiaoming Li, Xiaoguang Han, Tao Yang, and Shihui Guo. Real-world blind super-resolution via feature matching with implicit high-resolution priors. 2022.
- [6] Jooyoung Choi, Sungwon Kim, Yonghyun Jeong, Youngjune Gwon, and Sungroh Yoon. Ilvr: Conditioning method for denoising diffusion probabilistic models. In *2021 IEEE/CVF International Conference on Computer Vision (ICCV)*, pages 14347–14356, 2021.
- [7] Hyungjin Chung, Byeongsu Sim, and Jong Chul Ye. Come-closer-diffuse-faster: Accelerating conditional diffusion models for inverse problems through stochastic contraction. In *2022 IEEE/CVF Conference on Computer Vision and Pattern Recognition (CVPR)*, pages 12403–12412, 2022.

- [8] Trung Dao, Thuan Hoang Nguyen, Thanh Le, Duc Vu, Khoi Nguyen, Cuong Pham, and Anh Tran. Swiftbrush v2: Make your one-step diffusion model better than its teacher. In *Computer Vision – ECCV 2024*, pages 176–192, Cham, 2025. Springer Nature Switzerland.
- [9] Jia Deng, Wei Dong, Richard Socher, Li-Jia Li, Kai Li, and Li Fei-Fei. Imagenet: A large-scale hierarchical image database. In *2009 IEEE Conference on Computer Vision and Pattern Recognition*, pages 248–255, 2009.
- [10] Prafulla Dhariwal and Alexander Nichol. Diffusion models beat gans on image synthesis. In *Advances in Neural Information Processing Systems*, pages 8780–8794. Curran Associates, Inc., 2021.
- [11] Keyan Ding, Kede Ma, Shiqi Wang, and Eero P Simoncelli. Image quality assessment: Unifying structure and texture similarity. *IEEE transactions on pattern analysis and machine intelligence*, 44(5):2567–2581, 2020.
- [12] Chao Dong, Chen Change Loy, Kaiming He, and Xiaoou Tang. Image super-resolution using deep convolutional networks. *IEEE Transactions on Pattern Analysis and Machine Intelligence*, 38(2):295–307, 2016.
- [13] Chao Dong, Chen Change Loy, and Xiaoou Tang. Accelerating the super-resolution convolutional neural network. In *Computer Vision – ECCV 2016*, pages 391–407, Cham, 2016. Springer International Publishing.
- [14] Linwei Dong, Qingnan Fan, Yihong Guo, Zhonghao Wang, Qi Zhang, Jinwei Chen, Yawei Luo, and Changqing Zou. Tsd-sr: One-step diffusion with target score distillation for real-world image super-resolution. *arXiv preprint arXiv:2411.18263*, 2024.
- [15] Patrick Esser, Robin Rombach, and Björn Ommer. Taming transformers for high-resolution image synthesis. In *2021 IEEE/CVF Conference on Computer Vision and Pattern Recognition (CVPR)*, pages 12868–12878, 2021.
- [16] Daniel Glasner, Shai Bagon, and Michal Irani. Super-resolution from a single image. In *2009 IEEE 12th International Conference on Computer Vision*, pages 349–356, 2009.
- [17] Ian Goodfellow, Jean Pouget-Abadie, Mehdi Mirza, Bing Xu, David Warde-Farley, Sherjil Ozair, Aaron Courville, and Yoshua Bengio. Generative adversarial nets. In *Advances in Neural Information Processing Systems*. Curran Associates, Inc., 2014.
- [18] Nikita Gushchin, David Li, Daniil Selikhanovych, Evgeny Burnaev, Dmitry Baranchuk, and Alexander Korotin. Inverse bridge matching distillation. *arXiv preprint arXiv:2502.01362*, 2025.
- [19] Guande He, Kaiwen Zheng, Jianfei Chen, Fan Bao, and Jun Zhu. Consistency diffusion bridge models. In *Advances in Neural Information Processing Systems*, pages 23516–23548. Curran Associates, Inc., 2024.
- [20] Jonathan Ho, Ajay Jain, and Pieter Abbeel. Denoising diffusion probabilistic models. In *Advances in Neural Information Processing Systems*, pages 6840–6851. Curran Associates, Inc., 2020.
- [21] Edward J Hu, yelong shen, Phillip Wallis, Zeyuan Allen-Zhu, Yanzhi Li, Shean Wang, Lu Wang, and Weizhu Chen. LoRA: Low-rank adaptation of large language models. In *International Conference on Learning Representations*, 2022.
- [22] Zemin Huang, Zhengyang Geng, Weijian Luo, and Guo-jun Qi. Flow generator matching. *arXiv preprint arXiv:2410.19310*, 2024.
- [23] Andrey Ignatov, Nikolay Kobyshev, Radu Timofte, and Kenneth Vanhoey. Dslr-quality photos on mobile devices with deep convolutional networks. In *2017 IEEE International Conference on Computer Vision (ICCV)*, pages 3297–3305, 2017.
- [24] Michal Irani and Shmuel Peleg. Improving resolution by image registration. *Graphical Models and Image Processing*, 53:231–239, 1991.

- [25] Xiaozhong Ji, Yun Cao, Ying Tai, Chengjie Wang, Jilin Li, and Feiyue Huang. Real-world super-resolution via kernel estimation and noise injection. In *2020 IEEE/CVF Conference on Computer Vision and Pattern Recognition Workshops (CVPRW)*, pages 1914–1923, 2020.
- [26] Junjie Ke, Qifei Wang, Yilin Wang, Peyman Milanfar, and Feng Yang. Musiq: Multi-scale image quality transformer. In *2021 IEEE/CVF International Conference on Computer Vision (ICCV)*, pages 5128–5137, 2021.
- [27] Jiwon Kim, Jung Kwon Lee, and Kyoung Mu Lee. Accurate image super-resolution using very deep convolutional networks. In *2016 IEEE Conference on Computer Vision and Pattern Recognition (CVPR)*, pages 1646–1654, 2016.
- [28] Christian Ledig, Lucas Theis, Ferenc Huszár, Jose Caballero, Andrew Cunningham, Alejandro Acosta, Andrew Aitken, Alykhan Tejani, Johannes Totz, Zehan Wang, and Wenzhe Shi. Photo-realistic single image super-resolution using a generative adversarial network. In *2017 IEEE Conference on Computer Vision and Pattern Recognition (CVPR)*, pages 105–114, 2017.
- [29] Junnan Li, Dongxu Li, Silvio Savarese, and Steven Hoi. BLIP-2: Bootstrapping language-image pre-training with frozen image encoders and large language models. In *Proceedings of the 40th International Conference on Machine Learning*, pages 19730–19742. PMLR, 2023.
- [30] Yawei Li, Kai Zhang, Jingyun Liang, Jiezhang Cao, Ce Liu, Rui Gong, Yulun Zhang, Hao Tang, Yun Liu, Denis Demandolx, Rakesh Ranjan, Radu Timofte, and Luc Van Gool. Lsdir: A large scale dataset for image restoration. In *2023 IEEE/CVF Conference on Computer Vision and Pattern Recognition Workshops (CVPRW)*, pages 1775–1787, 2023.
- [31] Jingyun Liang, Jiezhang Cao, Guolei Sun, Kai Zhang, Luc Van Gool, and Radu Timofte. Swinir: Image restoration using swin transformer. In *2021 IEEE/CVF International Conference on Computer Vision Workshops (ICCVW)*, pages 1833–1844, 2021.
- [32] Jie Liang, Hui Zeng, and Lei Zhang. Details or artifacts: A locally discriminative learning approach to realistic image super-resolution. In *2022 IEEE/CVF Conference on Computer Vision and Pattern Recognition (CVPR)*, pages 5647–5656, 2022.
- [33] Jie Liang, Hui Zeng, and Lei Zhang. Efficient and degradation-adaptive network for real-world image super-resolution. In *Computer Vision – ECCV 2022*, pages 574–591, Cham, 2022. Springer Nature Switzerland.
- [34] Bee Lim, Sanghyun Son, Heewon Kim, Seungjun Nah, and Kyoung Mu Lee. Enhanced deep residual networks for single image super-resolution. In *2017 IEEE Conference on Computer Vision and Pattern Recognition Workshops (CVPRW)*, pages 1132–1140, 2017.
- [35] Xinqi Lin, Jingwen He, Ziyang Chen, Zhaoyang Lyu, Bo Dai, Fanghua Yu, Yu Qiao, Wanli Ouyang, and Chao Dong. Diffbir: Toward blind image restoration with generative diffusion prior. In *Computer Vision – ECCV 2024*, pages 430–448, Cham, 2025. Springer Nature Switzerland.
- [36] Guan-Hong Liu, Arash Vahdat, De-An Huang, Evangelos Theodorou, Weili Nie, and Anima Anandkumar. I²SB: Image-to-image schrödinger bridge. In *Proceedings of the 40th International Conference on Machine Learning*, pages 22042–22062. PMLR, 2023.
- [37] Haotian Liu, Chunyuan Li, Qingyang Wu, and Yong Jae Lee. Visual instruction tuning. In *Advances in Neural Information Processing Systems*, pages 34892–34916. Curran Associates, Inc., 2023.
- [38] Ilya Loshchilov and Frank Hutter. Decoupled weight decay regularization. In *International Conference on Learning Representations*, 2019.
- [39] Eric Luhman and Troy Luhman. Knowledge distillation in iterative generative models for improved sampling speed. *arXiv preprint arXiv:2101.02388*, 2021.
- [40] Weijian Luo, Tianyang Hu, Shifeng Zhang, Jiacheng Sun, Zhenguo Li, and Zhihua Zhang. Diff-instruct: A universal approach for transferring knowledge from pre-trained diffusion models. In *Advances in Neural Information Processing Systems*, pages 76525–76546. Curran Associates, Inc., 2023.

- [41] Ziwei Luo, Fredrik K. Gustafsson, Zheng Zhao, Jens Sjölund, and Thomas B. Schön. Image restoration with mean-reverting stochastic differential equations. In *Proceedings of the 40th International Conference on Machine Learning*, pages 23045–23066. PMLR, 2023.
- [42] Dustin Podell, Zion English, Kyle Lacey, Andreas Blattmann, Tim Dockhorn, Jonas Müller, Joe Penna, and Robin Rombach. SDXL: Improving latent diffusion models for high-resolution image synthesis. In *The Twelfth International Conference on Learning Representations*, 2024.
- [43] Robin Rombach, Andreas Blattmann, Dominik Lorenz, Patrick Esser, and Björn Ommer. High-resolution image synthesis with latent diffusion models. In *2022 IEEE/CVF Conference on Computer Vision and Pattern Recognition (CVPR)*, pages 10674–10685, 2022.
- [44] Chitwan Saharia, William Chan, Saurabh Saxena, Lala Li, Jay Whang, Emily L Denton, Kamyar Ghasemipour, Raphael Gontijo Lopes, Burcu Karagol Ayan, Tim Salimans, Jonathan Ho, David J Fleet, and Mohammad Norouzi. Photorealistic text-to-image diffusion models with deep language understanding. In *Advances in Neural Information Processing Systems*, pages 36479–36494. Curran Associates, Inc., 2022.
- [45] Chitwan Saharia, Jonathan Ho, William Chan, Tim Salimans, David J. Fleet, and Mohammad Norouzi. Image super-resolution via iterative refinement. *IEEE Transactions on Pattern Analysis and Machine Intelligence*, 45(4):4713–4726, 2023.
- [46] Mehdi S. M. Sajjadi, Bernhard Schölkopf, and Michael Hirsch. Enhancenet: Single image super-resolution through automated texture synthesis. In *2017 IEEE International Conference on Computer Vision (ICCV)*, pages 4501–4510, 2017.
- [47] Axel Sauer, Dominik Lorenz, Andreas Blattmann, and Robin Rombach. Adversarial diffusion distillation. In *Computer Vision – ECCV 2024*, pages 87–103, Cham, 2025. Springer Nature Switzerland.
- [48] Jascha Sohl-Dickstein, Eric Weiss, Niru Maheswaranathan, and Surya Ganguli. Deep unsupervised learning using nonequilibrium thermodynamics. In *Proceedings of the 32nd International Conference on Machine Learning*, pages 2256–2265, Lille, France, 2015. PMLR.
- [49] Jiaming Song, Chenlin Meng, and Stefano Ermon. Denoising diffusion implicit models. In *International Conference on Learning Representations*, 2021.
- [50] Yang Song and Stefano Ermon. Generative modeling by estimating gradients of the data distribution. In *Advances in Neural Information Processing Systems*. Curran Associates, Inc., 2019.
- [51] Yang Song, Jascha Sohl-Dickstein, Diederik P Kingma, Abhishek Kumar, Stefano Ermon, and Ben Poole. Score-based generative modeling through stochastic differential equations. In *International Conference on Learning Representations*, 2021.
- [52] Yang Song, Prafulla Dhariwal, Mark Chen, and Ilya Sutskever. Consistency models. In *Proceedings of the 40th International Conference on Machine Learning*, pages 32211–32252. PMLR, 2023.
- [53] Lingchen Sun, Rongyuan Wu, Zhengqiang Zhang, Hongwei Yong, and Lei Zhang. Improving the stability of diffusion models for content consistent super-resolution. *arXiv preprint arXiv:2401.00877*, 2024.
- [54] Jianyi Wang, Kelvin C.K. Chan, and Chen Change Loy. Exploring clip for assessing the look and feel of images. *Proceedings of the AAAI Conference on Artificial Intelligence*, 37(2): 2555–2563, 2023.
- [55] Jianyi Wang, Kelvin CK Chan, and Chen Change Loy. Exploring clip for assessing the look and feel of images. In *Proceedings of the AAAI conference on artificial intelligence*, pages 2555–2563, 2023.
- [56] Jianyi Wang, Zongsheng Yue, Shangchen Zhou, Kelvin C.K. Chan, and Chen Change Loy. Exploiting diffusion prior for real-world image super-resolution. *International Journal of Computer Vision*, 2024.

- [57] Xintao Wang, Ke Yu, Shixiang Wu, Jinjin Gu, Yihao Liu, Chao Dong, Yu Qiao, and Chen Change Loy. Esrgan: Enhanced super-resolution generative adversarial networks. In *Computer Vision – ECCV 2018 Workshops*, pages 63–79, Cham, 2019. Springer International Publishing.
- [58] Xintao Wang, Liangbin Xie, Chao Dong, and Ying Shan. Real-esrgan: Training real-world blind super-resolution with pure synthetic data. In *2021 IEEE/CVF International Conference on Computer Vision Workshops (ICCVW)*, pages 1905–1914, 2021.
- [59] Yufei Wang, Wenhan Yang, Xinyuan Chen, Yaohui Wang, Lanqing Guo, Lap-Pui Chau, Ziwei Liu, Yu Qiao, Alex C. Kot, and Bihan Wen. Sinsr: Diffusion-based image super-resolution in a single step. In *2024 IEEE/CVF Conference on Computer Vision and Pattern Recognition (CVPR)*, pages 25796–25805, 2024.
- [60] Zhou Wang, A.C. Bovik, H.R. Sheikh, and E.P. Simoncelli. Image quality assessment: from error visibility to structural similarity. *IEEE Transactions on Image Processing*, 13(4):600–612, 2004.
- [61] Zhengyi Wang, Cheng Lu, Yikai Wang, Fan Bao, Chongxuan LI, Hang Su, and Jun Zhu. Pro-lificdreamer: High-fidelity and diverse text-to-3d generation with variational score distillation. In *Advances in Neural Information Processing Systems*, pages 8406–8441. Curran Associates, Inc., 2023.
- [62] Pengxu Wei, Ziwei Xie, Hannan Lu, Zongyuan Zhan, Qixiang Ye, Wangmeng Zuo, and Liang Lin. Component divide-and-conquer for real-world image super-resolution. In *Computer Vision – ECCV 2020*, pages 101–117, Cham, 2020. Springer International Publishing.
- [63] Rongyuan Wu, Lingchen Sun, Zhiyuan Ma, and Lei Zhang. One-step effective diffusion network for real-world image super-resolution. In *Advances in Neural Information Processing Systems*, pages 92529–92553. Curran Associates, Inc., 2024.
- [64] Rongyuan Wu, Tao Yang, Lingchen Sun, Zhengqiang Zhang, Shuai Li, and Lei Zhang. Seesr: Towards semantics-aware real-world image super-resolution. In *2024 IEEE/CVF Conference on Computer Vision and Pattern Recognition (CVPR)*, pages 25456–25467, 2024.
- [65] Rui Xie, Ying Tai, Kai Zhang, Zhenyu Zhang, Jun Zhou, and Jian Yang. Addsr: Accelerating diffusion-based blind super-resolution with adversarial diffusion distillation, 2024.
- [66] Yanwu Xu, Yang Zhao, Zhisheng Xiao, and Tingbo Hou. Ufogen: You forward once large scale text-to-image generation via diffusion gans. In *Proceedings of the IEEE/CVF Conference on Computer Vision and Pattern Recognition*, pages 8196–8206, 2024.
- [67] Sidi Yang, Tianhe Wu, Shuwei Shi, Shanshan Lao, Yuan Gong, Mingdeng Cao, Jiahao Wang, and Yujiu Yang. Maniq: Multi-dimension attention network for no-reference image quality assessment. In *2022 IEEE/CVF Conference on Computer Vision and Pattern Recognition Workshops (CVPRW)*, pages 1190–1199, 2022.
- [68] Tao Yang, Rongyuan Wu, Peiran Ren, Xuansong Xie, and Lei Zhang. Pixel-aware stable diffusion for realistic image super-resolution and personalized stylization. In *Computer Vision – ECCV 2024*, pages 74–91, Cham, 2025. Springer Nature Switzerland.
- [69] Tianwei Yin, Michaël Gharbi, Taesung Park, Richard Zhang, Eli Shechtman, Fredo Durand, and Bill Freeman. Improved distribution matching distillation for fast image synthesis. In *Advances in Neural Information Processing Systems*, pages 47455–47487. Curran Associates, Inc., 2024.
- [70] Tianwei Yin, Michaël Gharbi, Richard Zhang, Eli Shechtman, Frédo Durand, William T. Freeman, and Taesung Park. One-step diffusion with distribution matching distillation. In *2024 IEEE/CVF Conference on Computer Vision and Pattern Recognition (CVPR)*, pages 6613–6623, 2024.
- [71] Fanghua Yu, Jinjin Gu, Zheyuan Li, Jinfan Hu, Xiangtao Kong, Xintao Wang, Jingwen He, Yu Qiao, and Chao Dong. Scaling up to excellence: Practicing model scaling for photo-realistic image restoration in the wild. In *2024 IEEE/CVF Conference on Computer Vision and Pattern Recognition (CVPR)*, pages 25669–25680, 2024.

- [72] Conghan Yue, Zhengwei Peng, Junlong Ma, Shiyang Du, Pengxu Wei, and Dongyu Zhang. Image restoration through generalized ornstein-uhlenbeck bridge. In *Proceedings of the 41st International Conference on Machine Learning*, pages 58068–58089. PMLR, 2024.
- [73] Zongsheng Yue, Jianyi Wang, and Chen Change Loy. Resshift: Efficient diffusion model for image super-resolution by residual shifting. In *Advances in Neural Information Processing Systems*, pages 13294–13307. Curran Associates, Inc., 2023.
- [74] Kai Zhang, Jingyun Liang, Luc Van Gool, and Radu Timofte. Designing a practical degradation model for deep blind image super-resolution. In *2021 IEEE/CVF International Conference on Computer Vision (ICCV)*, pages 4771–4780, 2021.
- [75] Lin Zhang, Lei Zhang, and Alan C Bovik. A feature-enriched completely blind image quality evaluator. *IEEE Transactions on Image Processing*, 24(8):2579–2591, 2015.
- [76] Lvmin Zhang, Anyi Rao, and Maneesh Agrawala. Adding conditional control to text-to-image diffusion models. In *2023 IEEE/CVF International Conference on Computer Vision (ICCV)*, pages 3813–3824, 2023.
- [77] Richard Zhang, Phillip Isola, Alexei A. Efros, Eli Shechtman, and Oliver Wang. The unreasonable effectiveness of deep features as a perceptual metric. In *2018 IEEE/CVF Conference on Computer Vision and Pattern Recognition*, pages 586–595, 2018.
- [78] Yulun Zhang, Kunpeng Li, Kai Li, Lichen Wang, Bineng Zhong, and Yun Fu. Image super-resolution using very deep residual channel attention networks. In *Computer Vision – ECCV 2018*, pages 294–310, Cham, 2018. Springer International Publishing.
- [79] Kaiwen Zheng, Guande He, Jianfei Chen, Fan Bao, and Jun Zhu. Diffusion bridge implicit models. *arXiv preprint arXiv:2405.15885*, 2024.
- [80] Mingyuan Zhou, Huangjie Zheng, Zhendong Wang, Mingzhang Yin, and Hai Huang. Score identity distillation: Exponentially fast distillation of pretrained diffusion models for one-step generation. In *Proceedings of the 41st International Conference on Machine Learning*, pages 62307–62331. PMLR, 2024.

Supplementary material and its structure

We organize the structure of supplementary materials as follows:

1. Appendix A discusses relation of RSD to relevant methods that involve training an auxiliary "fake" model - variational score distillation (VSD [61, 63, 70]), score identity distillation (SiD [80]), Flow Generator Matching (FGM [22]), and inverse bridge matching distillation (IBMD [18]). Appendix A.1 includes the derivation of variational score distillation for ResShift and its comparison with our RSD loss \mathcal{L}_θ . Appendix A.2 discusses the relation of RSD to SiD and FGM. Appendix A.3 discusses the relation of RSD to IBMD.
2. Appendix B details the correspondence between propositions and their implementation with the pseudocode of RSD. We also present the pseudocode for ResShift-VSD, introduced in Appendix A
3. Appendix C consists of experimental details for the implementation of RSD and baselines.
4. Appendix D consists of full quantitative results including additional baselines and results on full-size DRealSR, which haven't been shown in the main text due to space limitations.
5. Appendix E includes additional details of ResShift, which have not been shown in the main text due to space limitations.
6. Appendix G presents proofs of the main propositions in the paper.
7. Appendix F discusses the limitations of RSD, failure cases and potential societal impact.
8. Appendix H contains additional visual results for comparison between RSD and baselines.

A Relation of RSD to VSD, SiD, FGM and IBMD

A.1 Derivation of VSD objective for ResShift (ResShift-VSD) and comparative analysis with our objective

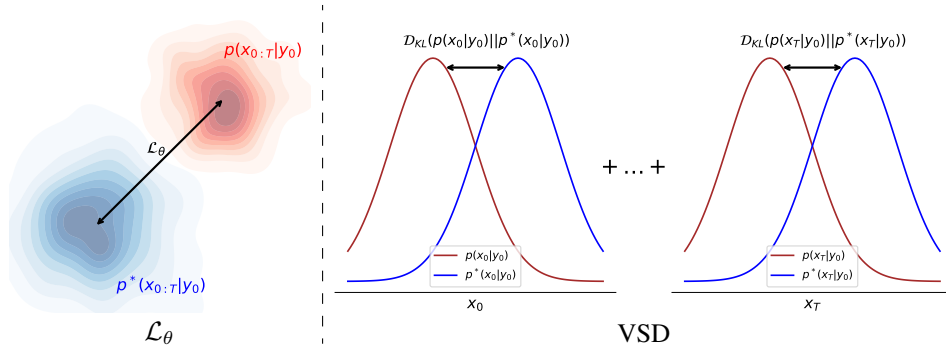


Figure 4: Illustration of the distinct distribution alignment strategies employed by the RSD \mathcal{L}_θ (**Ours**) and VSD loss functions. We denote by $p^*(x_{0:T}|y_0)$ reverse process of teacher ResShift model and by $p(x_{0:T}|y_0)$ reverse process of ResShift trained on generator G_θ data. The \mathcal{L}_θ loss enforces alignment of the joint distributions $p^*(x_{0:T}|y_0)$ and $p(x_{0:T}|y_0)$ across **all timesteps**, whereas the VSD loss aligns the marginal distributions at **each timestep t simultaneously** between distributions of teacher ResShift and ResShift trained on generator G_θ data. For formal derivations, see Eqs. (18) and (14).

In this section, we aim to: (1) derive the VSD loss in the ResShift framework to compare it with our distillation loss under the same experimental conditions (see Table 1 and Table 2); and (2) explain the main differences between our approach and the VSD loss. To achieve this, we consider a generator G_θ with parameters θ and seek an update rule for them. We use a fake ResShift model to solve the following problem:

$$\arg \min_f \sum_{t=1}^T w_t \mathbb{E}_{p_\theta(\hat{x}_0, y_0, x_t)} [\|f(x_t, y_0, t) - \hat{x}_0\|_2^2], \quad (10)$$

Since it is the optimization with MSE function, the solution is given by the conditional expectation:

$$f_{G_\theta}(x_t, y_0, t) = \mathbb{E}_{p_\theta(\hat{x}_0|y_0, x_t)}[\hat{x}_0]. \quad (11)$$

Notation. Further we will use the following notation:

- f^* – teacher ResShift.
- $x_{t_1:t_2} \stackrel{\text{def}}{=} (x_{t_1}, x_{t_1+1}, \dots, x_{t_2})$ and $dx_{t_1:t_2} \stackrel{\text{def}}{=} \prod_{t=t_1}^{t_2} dx_t$ for any integer $t_1 < t_2$.
- The joint distribution across all timesteps is defined as follows:

$$p(x_{0:T}|y_0) \stackrel{\text{def}}{=} p(x_T|y_0) \prod_{t=1}^T p(x_{t-1}|x_t, y_0). \quad (12)$$

The transition probabilities are determined using Eq. (2) and Eq. (4):

$$p(x_{t-1}|x_t, y_0) = \mathcal{N}\left(x_{t-1} \middle| \frac{\eta_{t-1}}{\eta_t} x_t + \frac{\alpha_t}{\eta_t} f_{G_\theta}(x_t, y_0, t), \kappa^2 \frac{\eta_{t-1}}{\eta_t} \alpha_t \mathbf{I}\right). \quad (13)$$

In the same way we define $p^*(x_{0:T}|y_0) \stackrel{\text{def}}{=} p^*(x_T|y_0) \prod_{t=1}^T p^*(x_{t-1}|x_t, y_0)$, where the transition probabilities are determined using f^* .

- $p^*(x_t|y_0) \stackrel{\text{def}}{=} \int p^*(x_{0:T}|y_0) dx_{0:t-1} dx_{t+1:T}$ and $p(x_t|y_0) \stackrel{\text{def}}{=} \int p(x_{0:T}|y_0) dx_{0:t-1} dx_{t+1:T}$ are marginal distributions.

Derivation of VSD loss for ResShift (ResShift-VSD). Initially, main objective of VSD loss [61, 63, 70] is:

$$\mathcal{L}_{\text{VSD}} = \mathbb{E}_{p(y_0)} \left[\sum_{t=1}^T w_t \mathcal{D}_{\text{KL}} \left(p(x_t|y_0) || p^*(x_t|y_0) \right) \right]. \quad (14)$$

We can get another expression for this loss using reparametrization based on the Eq. (21):

$$\begin{aligned} \mathcal{L}_{\text{VSD}} &= \sum_{t=1}^T w_t \mathbb{E}_{p(y_0)} \left[\mathcal{D}_{\text{KL}} \left(p(x_t|y_0) || p^*(x_t|y_0) \right) \right] = \sum_{t=1}^T w_t \mathbb{E}_{p(y_0)p(x_t|y_0)} \log \frac{p(x_t|y_0)}{p^*(x_t|y_0)} = \\ &= \sum_{t=1}^T w_t \mathbb{E}_{p(y_0)} \mathbb{E}_{\substack{x_t=(1-\eta_t)\hat{x}_0+\eta_t y_0+\kappa^2 \eta_t \epsilon' \\ \hat{x}_0=G_\theta(y_0, \epsilon) \\ \epsilon', \epsilon \sim \mathcal{N}(0; \mathbf{I})}} \log \frac{p(x_t|y_0)}{p^*(x_t|y_0)} \end{aligned} \quad (15)$$

Initially, this loss is intractable because it requires computing probability densities. However, taking the gradient facilitates its computation:

$$\begin{aligned} \nabla_\theta \mathcal{L}_{\text{VSD}} &= \\ &= - \sum_{t=1}^T w_t \mathbb{E}_{p(y_0)} \mathbb{E}_{\substack{x_t=(1-\eta_t)\hat{x}_0+\eta_t y_0+\kappa^2 \eta_t \epsilon' \\ \hat{x}_0=G_\theta(y_0, \epsilon) \\ \epsilon', \epsilon \sim \mathcal{N}(0; \mathbf{I})}} \left[(\nabla_{x_t} \log p^*(x_t|y_0) - \nabla_{x_t} \log p(x_t|y_0)) \frac{dx_t}{d\theta} \right] = \\ &= - \sum_{t=1}^T w_t \mathbb{E}_{p(y_0)} \mathbb{E}_{\substack{x_t=(1-\eta_t)\hat{x}_0+\eta_t y_0+\kappa^2 \eta_t \epsilon' \\ \hat{x}_0=G_\theta(y_0, \epsilon) \\ \epsilon', \epsilon \sim \mathcal{N}(0; \mathbf{I})}} \left[(\nabla_{x_t} \log p^*(x_t|y_0) - \nabla_{x_t} \log p(x_t|y_0)) \frac{dx_t}{d\hat{x}_0} \frac{d\hat{x}_0}{d\theta} \right] = \\ &= - \sum_{t=1}^T w'_t \mathbb{E}_{p(y_0)} \mathbb{E}_{\substack{x_t=(1-\eta_t)\hat{x}_0+\eta_t y_0+\kappa^2 \eta_t \epsilon' \\ \hat{x}_0=G_\theta(y_0, \epsilon) \\ \epsilon', \epsilon \sim \mathcal{N}(0; \mathbf{I})}} \left[(\nabla_{x_t} \log p^*(x_t|y_0) - \nabla_{x_t} \log p(x_t|y_0)) \frac{d\hat{x}_0}{d\theta} \right], \end{aligned} \quad (16)$$

where $w'_t \stackrel{\text{def}}{=} w_t \frac{dx_t}{d\hat{x}_0} = w_t(1 - \eta_t)$.

The expression $\nabla_{x_t} \log p(x_t|y_0)$ can be utilized as follows [79]:

$$\begin{aligned}\nabla_{x_t} \log p(x_t|y_0) &= \frac{\nabla_{x_t} p(x_t|y_0)}{p(x_t|y_0)} = \frac{\nabla_{x_t} \int q(x_t|y_0, x_0) p(x_0|y_0) dx_0}{p(x_t|y_0)} = \\ &= \frac{\int p(x_0|y_0) \nabla_{x_t} q(x_t|y_0, x_0) dx_0}{p(x_t|y_0)} = \frac{\int p(x_0|y_0) q(x_t|y_0, x_0) \nabla_{x_t} \log q(x_t|y_0, x_0) dx_0}{p(x_t|y_0)} = \\ &= \int \frac{p(x_0|y_0) q(x_t|y_0, x_0)}{p(x_t|y_0)} \nabla_{x_t} \log q(x_t|y_0, x_0) dx_0 = \int p(x_0|x_t, y_0) \nabla_{x_t} \log q(x_t|y_0, x_0) dx_0 \\ &= \mathbb{E}_{p(x_0|x_t, y_0)} \left[\nabla_{x_t} \log q(x_t|y_0, x_0) \right]\end{aligned}$$

Since $q(x_t|y_0, x_0) = \mathcal{N}(x_t|x_0 + \eta_t e_0, \kappa^2 \eta_t \mathbf{I})$ (See Eq. (21)), we get:

$$\nabla_{x_t} \log p(x_t|y_0) = - \mathbb{E}_{p(x_0|x_t, y_0)} \left[\frac{x_t - \eta_t y_0 - (1 - \eta_t) x_0}{\kappa^2 \eta_t} \right],$$

which leads to:

$$\nabla_{\theta} \mathcal{L}_{\text{VSD}} = - \sum_{t=1}^T w_t'' \mathbb{E}_{p(y_0)} \mathbb{E}_{\substack{x_t = (1-\eta_t)\hat{x}_0 + \eta_t y_0 + \kappa^2 \eta_t \epsilon' \\ \hat{x}_0 = G_{\theta}(y_0, \epsilon) \\ \epsilon', \epsilon \sim \mathcal{N}(0; \mathbf{I})}} \left[(f^*(x_t, y_0, t) - f_{G_{\theta}}(x_t, y_0, t)) \frac{d\hat{x}_0}{d\theta} \right] \quad (17)$$

where $w_t'' \stackrel{\text{def}}{=} w_t' \frac{1-\eta_t}{\kappa^2 \eta_t}$. As a result this loss can be implemented to match the gradients with $\nabla_{\theta} \mathcal{L}_{\text{VSD}}$ (see Algorithm 2). We call this model ResShift-VSD.

Reformulation of our \mathcal{L}_{θ} loss. We can express our RSD loss function as:

$$\mathcal{L}_{\theta} = \mathbb{E}_{p(y_0)} \left[\mathcal{D}_{\text{KL}} \left(p(x_{0:T}|y_0) \parallel p^*(x_{0:T}|y_0) \right) \right], \quad (18)$$

Recalling that the joint probability distribution can be factorized (see Eq. 12), the above loss can be decomposed as:

$$\begin{aligned}\mathcal{L}_{\theta} &= \mathbb{E}_{p(y_0)} \left[\mathcal{D}_{\text{KL}} \left(p(x_{0:T}|y_0) \parallel p^*(x_{0:T}|y_0) \right) \right] = \mathbb{E}_{p(y_0)} \left[\underbrace{\mathcal{D}_{\text{KL}} \left(p(x_T|y_0) \parallel p^*(x_T|y_0) \right)}_{=0 \text{ since } p(x_T|y_0) = p^*(x_T|y_0) \text{ from Eq. (21)}} \right] + \\ &\quad \mathbb{E}_{p(y_0)} \left[\sum_{t=1}^T \mathbb{E}_{p(x_t|y_0)} \mathcal{D}_{\text{KL}} \left(p(x_{t-1}|x_t, y_0) \parallel p^*(x_{t-1}|x_t, y_0) \right) \right].\end{aligned}$$

By applying Eq. (13), the KL divergence inside the expectation reduces to the KL divergence between Gaussian distributions, which can be computed in closed form. Consequently, we obtain:

$$\begin{aligned}\mathcal{L}_{\theta} &= \sum_{t=1}^T \mathbb{E}_{p(y_0)} \mathbb{E}_{p(x_t|y_0)} \mathcal{D}_{\text{KL}} \left(p(x_{t-1}|x_t, y_0) \parallel p^*(x_{t-1}|x_t, y_0) \right) \\ &= \sum_{t=1}^T \mathbb{E}_{p(y_0)} \mathbb{E}_{p(x_t|y_0)} \underbrace{\frac{1}{2\kappa^2} \frac{\alpha_t}{\eta_t \eta_{t-1}}}_{\stackrel{\text{def}}{=} w_t} \|f_{G_{\theta}}(x_t, y_0, t) - f^*(x_t, y_0, t)\|_2^2 \\ &= \sum_{t=1}^T w_t \mathbb{E}_{p(y_0)} \mathbb{E}_{p(x_t|y_0)} \|f_{G_{\theta}}(x_t, y_0, t) - f^*(x_t, y_0, t)\|_2^2.\end{aligned}$$

Since the distribution $p(x_t|y_0)$ is generally intractable, we instead use the tractable distribution $q(x_t|\hat{x}_0, y_0)$, which is known to satisfy $q(x_t|\hat{x}_0, y_0) = p(x_t|y_0)$. Thus, we have:

$$\mathcal{L}_{\theta} = \sum_{t=1}^T w_t \mathbb{E}_{p(y_0)} \mathbb{E}_{q(x_t|\hat{x}_0, y_0)} \|f_{G_{\theta}}(x_t, y_0, t) - f^*(x_t, y_0, t)\|_2^2.$$

Noting that the integrand is independent of \hat{x}_0 , so we can use $p_\theta(\hat{x}_0, y_0)$ instead of $p(y_0)$, since $\int p_\theta(\hat{x}_0|y_0)d\hat{x}_0 = 1$, and therefore we obtain the following:

$$\mathcal{L}_\theta = \sum_{t=1}^T w_t \mathbb{E}_{q(x_t|\hat{x}_0, y_0) p_\theta(\hat{x}_0, y_0)} \|f_{G_\theta}(x_t, y_0, t) - f^*(x_t, y_0, t)\|_2^2.$$

Finally, recognizing that the joint distribution $p_\theta(\hat{x}_0, y_0, x_t)$ is defined as

$$p_\theta(\hat{x}_0, y_0, x_t) \stackrel{\text{def}}{=} q(x_t|\hat{x}_0, y_0) p_\theta(\hat{x}_0, y_0),$$

we arrive at the final form of the RSD loss:

$$\mathcal{L}_\theta = \sum_{t=1}^T w_t \mathbb{E}_{p_\theta(\hat{x}_0, y_0, x_t)} \|f_{G_\theta}(x_t, y_0, t) - f^*(x_t, y_0, t)\|_2^2.$$

This derivation demonstrates that the loss function in Eq. (18) reconstructs the initial objective presented in Eq. (6).

Conceptual comparison of VSD and our RSD \mathcal{L}_θ losses. The key difference between the VSD and \mathcal{L}_θ losses lies in how they match distributions. For a more clear intuitive explanation one can see formulations of losses with \mathcal{D}_{KL} for VSD (Eq. (14)) and \mathcal{L}_θ (Eq. (18)). The VSD loss aligns the marginal distributions at each timestep t between the teacher’s and fake’s distributions. In contrast, the \mathcal{L}_θ loss matches the joint distribution across all timesteps. This difference is illustrated in Figure 4, where the \mathcal{L}_θ loss enforces joint distribution alignment, while the VSD loss aligns marginal distributions separately and then sums them.

RSD loss is superior to VSD loss for SR problem because it aligns the joint distribution across all timesteps, ensuring a more holistic match between teacher and student models. Unlike VSD, which aligns marginal distributions at each timestep separately, RSD captures temporal dependencies more effectively. This joint alignment is particularly beneficial for SR tasks, where maintaining consistency and accuracy across all image details and features is crucial for high-quality resolution. The RSD loss, by considering the entire distribution over multiple timesteps, leads to more precise and stable SR performance.

Computational analysis of VSD and \mathcal{L}_θ losses. As was shown in Proposition 3.1, our loss can be evaluated via:

$$\mathcal{L}_\theta = -\min_{\phi} \left\{ \sum_{t=1}^T w_t \mathbb{E}_{p_\theta(\hat{x}_0, x_t, y_0)} \left[\|f_\phi(x_t, y_0, t)\|_2^2 - \|f^*(x_t, y_0, t)\|_2^2 + 2\langle f^*(x_t, y_0, t) - f_\phi(x_t, y_0, t), \hat{x}_0 \rangle \right] \right\}.$$

Using Eq. (11) we can rewrite it and make reparameterization:

$$\begin{aligned} \mathcal{L}_\theta &= -\sum_{t=1}^T w_t \mathbb{E}_{p_\theta(\hat{x}_0, x_t, y_0)} \left[\|f_{G_\theta}(x_t, y_0, t)\|_2^2 - \|f^*(x_t, y_0, t)\|_2^2 + 2\langle f^*(x_t, y_0, t) - f_{G_\theta}(x_t, y_0, t), \hat{x}_0 \rangle \right] = \\ &= -\sum_{t=1}^T w_t \mathbb{E}_{\substack{x_t = (1-\eta_t)\hat{x}_0 + \eta_t y_0 + \kappa^2 \eta_t \epsilon' \\ \hat{x}_0 = G_\theta(y_0, \epsilon) \\ \epsilon', \epsilon \sim \mathcal{N}(0; \mathbf{I})}} \left[\|f_{G_\theta}(x_t, y_0, t)\|_2^2 - \|f^*(x_t, y_0, t)\|_2^2 + 2\langle f^*(x_t, y_0, t) - f_{G_\theta}(x_t, y_0, t), \hat{x}_0 \rangle \right]. \end{aligned}$$

To compare it with VSD loss, we can take the gradient of \mathcal{L}_θ loss and get:

$$\frac{d\mathcal{L}_\theta}{d\theta} = -\sum_{t=1}^T w_t \mathbb{E}_{\substack{x_t = (1-\eta_t)\hat{x}_0 + \eta_t y_0 + \kappa^2 \eta_t \epsilon' \\ \hat{x}_0 = G_\theta(y_0, \epsilon) \\ \epsilon', \epsilon \sim \mathcal{N}(0; \mathbf{I})}} \left[\frac{d\|f_{G_\theta}(x_t, y_0, t)\|_2^2}{d\theta} - \frac{d\|f^*(x_t, y_0, t)\|_2^2}{d\theta} + \right]$$

$$\begin{aligned}
& 2\left\langle \frac{df^*(x_t, y_0, t)}{d\theta} - \frac{df_{G_\theta}(x_t, y_0, t)}{d\theta}, \hat{x}_0 \right\rangle + 2\left\langle f^*(x_t, y_0, t) - f_{G_\theta}(x_t, y_0, t), \frac{d\hat{x}_0}{d\theta} \right\rangle = \\
& - \sum_{t=1}^T w_t \mathbb{E}_{\substack{x_t = (1-\eta_t)\hat{x}_0 + \eta_t y_0 + \kappa^2 \eta_t \epsilon' \\ \hat{x}_0 = G_\theta(y_0, \epsilon) \\ \epsilon', \epsilon \sim \mathcal{N}(0; \mathbf{I})}} \left[\frac{d\|f_{G_\theta}(x_t, y_0, t)\|_2^2}{d\theta} - \frac{d\|f^*(x_t, y_0, t)\|_2^2}{d\theta} + \right. \\
& \qquad \qquad \qquad \left. 2\left\langle \frac{df^*(x_t, y_0, t)}{d\theta} - \frac{df_{G_\theta}(x_t, y_0, t)}{d\theta}, \hat{x}_0 \right\rangle \right] \\
& - \sum_{t=1}^T w_t \mathbb{E}_{\substack{x_t = (1-\eta_t)\hat{x}_0 + \eta_t y_0 + \kappa^2 \eta_t \epsilon' \\ \hat{x}_0 = G_\theta(y_0, \epsilon) \\ \epsilon', \epsilon \sim \mathcal{N}(0; \mathbf{I})}} \left[2\left\langle f^*(x_t, y_0, t) - f_{G_\theta}(x_t, y_0, t), \frac{d\hat{x}_0}{d\theta} \right\rangle \right] \\
& \underbrace{\hspace{15em}}_{= 2 \cdot \nabla_\theta \mathcal{L}_{\text{VSD}} \text{ up to weighting term } w_t \text{ (see Eq.(17))}}
\end{aligned}$$

Consequently, the gradients of the our RSD \mathcal{L}_θ loss function encompass those of the VSD loss, scaled by a constant factor of 2 and modulated by the time-dependent weighting term w_t . These scaling factors do not affect the optimal solution of the loss. However, \mathcal{L}_θ additionally incorporates gradient contributions from both the teacher and the fake models. To reduce \mathcal{L}_θ to the standard VSD formulation, the application of a stop-gradient operator is required to suppress the influence of these auxiliary gradient terms. For a detailed implementation, refer to Algorithm 2.

A.2 Relation of RSD to SiD and FGM

The loss function \mathcal{L}_θ can be reformulated as follows:

$$\begin{aligned}
\mathcal{L}_\theta &= \min_{\phi} \left\{ \sum_{t=1}^T w_t \mathbb{E}_{p_\theta(\hat{x}_0, y_0, x_t)} \left(\|f^*(x_t, y_0, t)\|_2^2 - \|f_\phi(x_t, y_0, t)\|_2^2 + \right. \right. \\
& \quad \left. \left. 2\langle f_\phi(x_t, y_0, t) - f^*(x_t, y_0, t), \hat{x}_0 \rangle \right) \right\} \\
&= \min_{\phi} \left\{ \sum_{t=1}^T w_t \mathbb{E}_{p_\theta(\hat{x}_0, y_0, x_t)} \left(\|f^*(x_t, y_0, t)\|_2^2 - \|f_\phi(x_t, y_0, t)\|_2^2 + \right. \right. \\
& \quad \left. \left. 2\langle f_\phi(x_t, y_0, t) - f^*(x_t, y_0, t), \hat{x}_0 \rangle \pm 2\langle f^*(x_t, y_0, t), f_\phi(x_t, y_0, t) \rangle \pm \|f_\phi(x_t, y_0, t)\|_2^2 \right) \right\} \\
&= \min_{\phi} \left\{ \sum_{t=1}^T w_t \mathbb{E}_{p_\theta(\hat{x}_0, y_0, x_t)} \left(\|f^*(x_t, y_0, t) - f_\phi(x_t, y_0, t)\|_2^2 + \right. \right. \\
& \quad \left. \left. 2\langle f^*(x_t, y_0, t) - f_\phi(x_t, y_0, t), f_\phi(x_t, y_0, t) \rangle + 2\langle f_\phi(x_t, y_0, t) - f^*(x_t, y_0, t), \hat{x}_0 \rangle \right) \right\} \\
&= \min_{\phi} \left\{ \sum_{t=1}^T w_t \mathbb{E}_{p_\theta(\hat{x}_0, y_0, x_t)} \left(\|f^*(x_t, y_0, t) - f_\phi(x_t, y_0, t)\|_2^2 + \right. \right. \\
& \quad \left. \left. 2\langle f^*(x_t, y_0, t) - f_\phi(x_t, y_0, t), f_\phi(x_t, y_0, t) - \hat{x}_0 \rangle \right) \right\}
\end{aligned}$$

One can see that our objective can be reformulated in a manner closely resembling the formulations employed in SiD [80, Eq. 23 with $\alpha = 0.5$] and FGM [22, Eqs. 4.11–4.12] with up to time weighting w_t . However, in both SiD (where $\alpha = 1.0, 1.2$ were used in the experiments) and FGM, the authors either omitted the quadratic term or assigned it a negative coefficient in image-based experiments due to the instability it introduced. In contrast to these approaches, we retain the complete original loss formulation as prescribed by theory, without discarding or modifying any of its components.

Furthermore, it is important to emphasize that SiD and FGM were primarily developed for image generation tasks, whereas our proposed RSD framework is specifically tailored for image restoration, with a focus on reconstructing high-resolution images from their low-resolution counterparts. To this end, we adopt a dedicated ResShift architecture that integrates both VAE and U-Net components, along with a diffusion process specifically designed for the super-resolution task. Additionally, we incorporate supervised loss terms tailored to the super-resolution objective (see Section 3.5). These

task-specific design choices stand in contrast to SiD and FGM, which lack such adaptations for image restoration scenarios.

A.3 Relation of RSD to IBMD

The loss function \mathcal{L}_θ can be equivalently reformulated in the following manner:

$$\begin{aligned}
\mathcal{L}_\theta &= \min_{\phi} \left\{ \sum_{t=1}^T w_t \mathbb{E}_{p_\theta(\hat{x}_0, y_0, x_t)} \left(\|f^*(x_t, y_0, t)\|_2^2 - \|f_\phi(x_t, y_0, t)\|_2^2 + \right. \right. \\
&\quad \left. \left. 2\langle f_\phi(x_t, y_0, t) - f^*(x_t, y_0, t), \hat{x}_0 \rangle \right) \right\} \\
&= \min_{\phi} \left\{ \sum_{t=1}^T w_t \mathbb{E}_{p_\theta(\hat{x}_0, y_0, x_t)} \left(\|f^*(x_t, y_0, t)\|_2^2 - \|f_\phi(x_t, y_0, t)\|_2^2 + \right. \right. \\
&\quad \left. \left. 2\langle f_\phi(x_t, y_0, t), \hat{x}_0 \rangle - 2\langle f^*(x_t, y_0, t), \hat{x}_0 \rangle \pm \|\hat{x}_0\|_2^2 \right) \right\} \\
&= \min_{\phi} \left\{ \sum_{t=1}^T w_t \mathbb{E}_{p_\theta(\hat{x}_0, y_0, x_t)} \left(\|f^*(x_t, y_0, t) - \hat{x}_0\|_2^2 - \|f_\phi(x_t, y_0, t) - \hat{x}_0\|_2^2 \right) \right\} \\
&= \sum_{t=1}^T w_t \mathbb{E}_{p_\theta(\hat{x}_0, y_0, x_t)} \left(\|f^*(x_t, y_0, t) - \hat{x}_0\|_2^2 - \min_{\phi} \left\{ \|f_\phi(x_t, y_0, t) - \hat{x}_0\|_2^2 \right\} \right) \quad (19)
\end{aligned}$$

It is worth noting that our RSD loss, denoted by \mathcal{L}_θ , can be interpreted as a discrete variant of the inverse bridge matching distillation (IBMD) loss [18, Eq. 10], originally proposed for conditional Bridge Matching models. From a theoretical perspective, one of our main contributions is the development of a discretized form of the IBMD-conditional loss, which can offer practical benefits for tasks such as super-resolution.

While the IBMD framework has been applied to a broad range of problems, including image restoration, its experimental setup relied on relatively simplistic degradation processes, such as bicubic and pool. In contrast, we have tailored our objective specifically for image restoration by integrating it into the ResShift paradigm, incorporating additional supervised losses explicitly designed for real-world super-resolution (see Section 3.5), and utilizing a more challenging and realistic degradation model based on Real-ESRGAN. We also note that ResShift and RSD use VAE and a diffusion process in the latent space, while IBMD operates in the pixel space, which makes RSD more efficient and scalable for handling images of varying resolutions due to the reduced computational complexity and memory requirements in the latent domain. Another relevant difference between implementations of IBMD and ResShift for the SR problem is the bigger architecture of IBMD. IBMD for super-resolution uses ADM architecture [10] following I2SB [36] with 552M parameters, while RSD follows ResShift architecture with 174M parameters.

Thus, in addition to our theoretical contribution, we extend the implementation of the IBMD loss to more severe and practically relevant degradation settings. These task-specific modifications differentiate our approach from the original IBMD formulation, which does not account for such adaptations in the context of real-world image restoration scenarios.

B Algorithm of RSD

The pseudocode for our RSD training algorithm is presented in Algorithm 1.

Algorithm 1: Residual Shifting Distillation (RSD).

Input:

Training dataset $p_{\text{data}}(x_0, y_0)$;

Pretrained ResShift Teacher model f^* ; frozen encoder and decoder of VAE: Enc, Dec;

Number of fake ResShift (f_ϕ) training iterations K , f_ϕ^{encoder} - encoder part of fake ResShift model;

Output:

A trained generator G_θ ;

```

1 func SampleEverything()
2   Sample  $(x_0, y_0) \sim p_{\text{data}}(x_0, y_0)$ 
3    $z_y \leftarrow \text{Enc}(\text{upsample}(y_0))$ ;  $z_0 \leftarrow \text{Enc}(x_0)$ 
4   Sample  $t_n \sim \mathcal{U}\{1, \dots, T\}$ ,  $z_{t_n} \sim q(z_{t_n}|z_0, z_y)$ ,  $\epsilon \sim \mathcal{N}(0, \mathbf{I})$  // Eq. (21)
5    $\hat{z}_0^{t_n} \leftarrow G_\theta(z_{t_n}, y_0, t_n, \epsilon)$ 
6   Sample  $t \sim \mathcal{U}\{1, \dots, T\}$ ,  $z_t \sim q(z_t|\hat{z}_0^{t_n}, z_y)$  // Eq. (21)
7   return  $(x_0, y_0, z_0, z_y, t_n, z_{t_n}, \hat{z}_0^{t_n}, t, z_t)$ 
8
9 // Initialize generator from pretrained model
10 // Initialize fake ResShift from pretrained model
11 // and GAN discriminator head randomly
12  $G_\theta \leftarrow \text{copyWeightsAndUnfreeze}(f^*)$ ;
13  $f_\phi \leftarrow \text{copyWeightsAndUnfreezeAndAddNoiseChannels}(f^*)$  // See Appendix C
14  $D_\psi \leftarrow \text{randomInitOfDiscriminatorHead}()$ 
15
16 while train do
17   // Train fake ResShift model
18   for  $k \leftarrow 1$  to  $K$  do
19      $(x_0, y_0, z_0, z_y, t_n, z_{t_n}, \hat{z}_0^{t_n}, t, z_t) \leftarrow \text{SampleEverything}()$  // Generate training data
20      $\mathcal{L}_{\text{fake}} \leftarrow w_t \|f_\phi(z_t, y_0, t) - \hat{z}_0^{t_n}\|_2^2$  // Eq. (5)
21      $\mathcal{L}_{\text{GAN}} \leftarrow \text{calcGANLossD}(D_\psi(f_\phi^{\text{encoder}}(\hat{z}_0^{t_n}, y_0, 0)), D_\psi(f_\phi^{\text{encoder}}(z_0, y_0, 0)))$  // Eq. (8)
22      $\mathcal{L}_\phi^{\text{total}} \leftarrow \mathcal{L}_{\text{fake}} + \lambda_2 \mathcal{L}_{\text{GAN}}$  // Eq. (9)
23     Update  $\phi$  by using  $\frac{\partial \mathcal{L}_\phi^{\text{total}}}{\partial \phi}$ 
24     Update  $\psi$  by using  $\frac{\partial \mathcal{L}_{\text{GAN}}}{\partial \psi}$ 
25   end for
26   // Train generator model
27   // Generate training data
28    $(x_0, y_0, z_0, z_y, t_n, z_{t_n}, \hat{z}_0^{t_n}, t, z_t) \leftarrow \text{SampleEverything}()$ 
29
30   // Compute  $\mathcal{L}_\theta$  loss
31    $\mathcal{L}_\theta \leftarrow \text{calcThetaLoss}(f^*(z_t, y_0, t), f_\phi(z_t, y_0, t), \hat{z}_0^{t_n})$  // Eq. (7)
32
33   // Compute  $\mathcal{L}_{\text{LPIPS}}$  loss
34   Sample  $z_T \sim \mathcal{N}(z_T|z_y, \kappa^2 \mathbf{I})$  // Eq. (21)
35    $\hat{z}_0 \leftarrow G_\theta(z_T, y_0, T, \epsilon)$ 
36    $\mathcal{L}_{\text{LPIPS}} \leftarrow \text{LPIPS}(x_0, \text{Dec}(\hat{z}_0))$ 
37
38   // Compute generator  $\mathcal{L}_{\text{GAN}}$  loss
39    $\mathcal{L}_{\text{GAN}} \leftarrow \text{calcGANLossG}(D_\psi(f_\phi^{\text{encoder}}(\hat{z}_0^{t_n}, y_0, 0)))$  // Eq. (8)
40
41    $\mathcal{L}_\theta^{\text{total}} \leftarrow \mathcal{L}_\theta + \lambda_1 \mathcal{L}_{\text{LPIPS}} + \lambda_2 \mathcal{L}_{\text{GAN}}$  // Eq. (9)
42   Update  $\theta$  by using  $\frac{\partial \mathcal{L}_\theta^{\text{total}}}{\partial \theta}$ 
43 end while

```

The pseudocode for the baseline ResShift-VSD training algorithm is presented in Algorithm 2, while the foundational theoretical framework is detailed in Appendix A.1. To ensure a fair comparison with the distillation loss in OSEDiff [63], specifically the VSD Loss, under an identical experimental setup (i.e., ResShift), we adapted it to the ResShift framework using the same implementation details.

Algorithm 2: ResShift-VSD.

Input:

Training dataset $p_{\text{data}}(x_0, y_0)$;
 Pretrained ResShift Teacher model f^* ; frozen encoder and decoder of VAE: Enc, Dec;
 Number of fake ResShift (f_ϕ) training iterations K ;

Output:

A trained generator G_θ ;

```

1 func SampleEverything()
2   Sample  $(x_0, y_0) \sim p_{\text{data}}(x_0, y_0)$ ;
3    $z_y \leftarrow \text{Enc}(\text{upsample}(y_0))$ 
4   Sample  $z_T \sim \mathcal{N}(z_y, \kappa^2 \eta_T \mathbf{I})$  // Eq. (21)
5    $\hat{z}_0 \leftarrow G_\theta(z_T, y_0, T)$ 
6   Sample  $t \sim \mathcal{U}\{1, \dots, T\}$ ,  $z_t \sim q(z_t | \hat{z}_0, z_y)$  // Eq. (21)
7   return  $(y_0, t, z_t, \hat{z}_0)$ 
8
9 // Initialize generator from pretrained model
10 // Initialize fake ResShift from pretrained model
11  $G_\theta \leftarrow \text{copyWeightsAndUnfreeze}(f^*)$ ;
12  $f_\phi \leftarrow \text{copyWeightsAndUnfreeze}(f^*)$ ;
13
14 while train do
15   // Train fake ResShift model
16   for  $k \leftarrow 1$  to  $K$  do
17      $(y_0, t, z_t, \hat{z}_0) \leftarrow \text{SampleEverything}()$  // Generate training data
18      $\mathcal{L}_{\text{fake}} \leftarrow w_t \|f_\phi(z_t, y_0, t) - \hat{z}_0\|_2^2$  // Eq. (5)
19     Update  $\phi$  by using  $\frac{\partial \mathcal{L}_{\text{fake}}}{\partial \phi}$ 
20   end for
21
22   // Train generator model
23    $(y_0, t, z_t, \hat{z}_0) \leftarrow \text{SampleEverything}()$  // Generate training data
24    $\mathcal{L}_\theta \leftarrow \text{calcThetaLoss}(\text{stopgrad}(f^*(z_t, y_0, t)), \text{stopgrad}(f_\phi(z_t, y_0, t)), \hat{z}_0)$  // Eq. (7)
25   Update  $\theta$  by using  $\frac{\partial \mathcal{L}_\theta}{\partial \theta}$ 
26 end while

```

C Experiments details

Noise condition. By default, fake ResShift and generator models are initialized with teacher weights. Furthermore, for noise conditioning, as described in §3.2, we implement an additional convolutional channel to expand the generator’s first convolutional layer to accept noise as an additional input. The noise is concatenated with the encoded low-resolution image and is processed by a separate zero-initialized convolutional layer.

Training hyperparameters. We use the same hyperparameters as SinSR for training, including the batch size, EMA rate, and optimizer type. To achieve smoother convergence, we replace the learning rate scheduler with a constant learning rate of 5×10^{-5} , matching the base learning rate of SinSR. Additionally, we adjust the AdamW [38] optimizer’s β parameters to $[0.9, 0.95]$ to further stabilize training. To ensure controlled adaptation between the generator and the fake ResShift models, we update the generator’s weights once for every $K = 5$ updates of the fake model, following the strategy of DMD2 [69]. Furthermore, we adopt the loss normalization technique proposed in [80] to improve training stability. In the final loss function (Eq. 9), we set $\lambda_1 = 2$ and $\lambda_2 = 3 \cdot 10^{-3}$ following OSEDiff [63] and DMD2, respectively.

Training time. The complete training process, performed on 4 NVIDIA A100 GPUs, takes approximately 5 hours. During this time, the student model undergoes around 3000 gradient update iterations, while the fake model completes 15000 iterations.

Codebase. Our method is implemented based on the original SinSR repository [59], which serves as the primary code source for our experiments. We build upon this framework to integrate our training algorithm, which is described in Appendix B.

Datasets and baselines. Table 7 lists details on the datasets used for training and testing, including their sources, download links, and associated licenses. Table 8 lists the models used for training and quality comparison and links to access them.

Metrics calculation of SR models. For calculating SR metrics, we use PyTorch Toolbox for Image Quality Assessment and pyiqa package [4]. We also used the image quality assessment script provided in the OSEDiff GitHub repository.

Table 7: The used datasets and their licenses.

Name	URL	Citation	License
RealSR-V3	GitHub Link	[3]	ODbL v1
RealSet65	GitHub Link	[73]	NTU S-Lab License 1.0
DRealSR	GitHub Link	[62]	Unknown
ImageNet	Website Link	[9]	Custom (research, non-commercial)
ImageNet-Test	Google Drive Link	[73]	NTU S-Lab License
DIV2K-Val-512	Hugging Face Link	[1, 56]	NTU S-Lab License
DRealSR-512	Hugging Face Link	[56, 62]	NTU S-Lab License
RealSR-512	Hugging Face Link	[3, 56]	NTU S-Lab License

Table 8: Baselines used for comparison. In each case, we used original code from GitHub repositories and model weights.

Name	URL	Citation	License
Real-ESRGAN	GitHub Link	[58]	BSD 3-Clause License
BSRGAN	GitHub Link	[74]	Apache-2.0 license
SwinIR	GitHub Link	[31]	Apache-2.0 license
ResShift	GitHub Link	[73]	S-Lab License 1.0
SinSR	GitHub Link	[59]	CC BY-NC-SA 4.0
SUPIR	GitHub Link	[71]	SUPIR Software License
OSEDiff	GitHub Link	[63]	Apache License 2.0

D Additional quantitative results

We present an additional set of quantitative results, including more baselines and evaluations on full-size DRealSR images [62], which were not included in the main text due to space limitations:

- Table 9 provides results on full-size images from the DRealSR dataset [62].
- Table 10 presents an extension version of Table 1 on RealSR [3] and RealSet65 [73] datasets with additional baselines.
- Table 11 presents an extension version of Table 2 on the ImageNet-Test dataset [73] with additional baselines.
- Table 12 presents an extension version of Table 3 on crops from DIV2K [1], RealSR, and DRealSR used in StableSR [56] with additional baselines.

Table 9. We evaluated the following models for Table 9 and followed their official implementations listed in Table 8:

1. **Diffusion-based SR models.** We ran pre-trained models of ResShift [73], SinSR [59], OSediff [63], and SUPIR [71] as representative members of diffusion-based SR models. We used the following checkpoints from the respective official repositories listed in Table 8: `resshift_realsrx4_s15_v1.pth`, `SinSR_v2.pth`, `osediff.pkl`, and `SUPIR-v0Q.ckpt`. Due to the high resolution of DRealSR images and the high demands for GPU memory for the SUPIR model, we ran it with tiled VAE using the flag `-use_tile_vae`.
2. **GAN-based SR models.** We ran pre-trained Real-ESRGAN [58] and BSRGAN [74] GAN-based SR models with the checkpoint names `RealESRGAN_x4plus.pth` and `BSRGAN.pth`, provided in the respective GitHub repositories listed in Table 8.
3. **Transformer-based SR models.** We ran pre-trained SwinIR model [31] with the checkpoint name `003_realSR_BSRGAN_DFOWMFC_s64w8_SwinIR-L_x4_GAN.pth` as the representative model from transformer-based SR models using the respective GitHub repository listed in Table 8.

We compute the same set of metrics as in Table 3 - PSNR, SSIM, LPIPS, CLIPQA, MUSIQ, DISTS, NIQE, and MANIQA-PIPAL.

Table 10 . We report an extended version of Table 1 with additional baselines used in ResShift and SinSR papers:

1. **GAN-based SR models.** We evaluated Real-ESRGAN [58] and BSRGAN [74] on RealSR and RealSet65.
2. **SwinIR.** We also evaluated SwinIR on RealSR and RealSet65.

Table 11 . We report an extended version of Table 2 with additional baselines used in ResShift and SinSR papers:

1. **Diffusion-based SR models.** We borrow the results of Table 2 from SinSR for LDM-15 and LDM-30 [43], and SinSR [59]. We borrow the results of Table 3 from [73] for ResShift.
2. **GAN-based SR models.** We borrow the results of Table 2 from SinSR for ESRGAN [57], RealSR-JPEG [25], Real-ESRGAN [58], BSRGAN [74].
3. **DASR and SwinIR.** We also borrow the results of Table 2 from SinSR for DASR [33] and SwinIR [31].

Table 12 . We report an extended version of Table 3 with additional baselines used in the OSediff paper:

1. **Diffusion-based SR models.** We borrow the results of Table 1 from OSediff for StableSR [56], DiffBIR [35], SeeSR [64], PASD [68], ResShift [73], and SinSR [59].
2. **GAN-based SR models.** We borrow the results of Table 1 from OSediff for Real-ESRGAN [58], BSRGAN [74], LDL [32], and FeMASR [5].

These results demonstrate that our RSD model achieves performance comparable to state-of-the-art models across a broad range of metrics and methods.

Table 9: Quantitative results of models on full size images from DRealSR [62]. The best and second best results are highlighted in **bold** and underline.

Methods	NFE	PSNR \uparrow	SSIM \uparrow	LPIPS \downarrow	CLIPQA \uparrow	MUSIQ \uparrow	DISTS \downarrow	NIQE \downarrow	MANIQA \uparrow
ResShift [73]	15	28.76	0.7863	0.4310	0.5838	32.042	0.2314	6.6335	0.4297
SinSR [59]	1	27.32	0.7233	0.4452	0.7223	32.800	0.2368	5.5748	0.4757
OSDiff [63]	1	26.67	0.7922	0.3123	<u>0.7264</u>	<u>37.761</u>	0.1617	4.1768	0.5883
SUPIR [71]	50	25.73	0.7224	0.3906	0.5862	36.089	0.1944	<u>4.4685</u>	<u>0.5720</u>
Real-ESRGAN [58]	1	27.91	<u>0.8249</u>	<u>0.2818</u>	0.5180	35.255	<u>0.1464</u>	4.7142	0.4756
BSRGAN [74]	1	<u>28.34</u>	0.8206	0.2929	0.5704	35.500	0.1636	4.6811	0.4682
SwinIR [31]	1	28.31	0.8272	0.2741	0.5072	35.826	0.1387	4.6665	0.4617
RSD (Ours)	1	27.66	0.7864	0.3105	0.7398	38.340	0.1868	4.6098	0.5314

Table 10: Extended quantitative results of models on two real-world datasets. The best and second best results are highlighted in **bold** and underline.

Methods	NFE	Datasets						
		<i>RealSR</i>					<i>RealSet65</i>	
		PSNR \uparrow	SSIM \uparrow	LPIPS \downarrow	CLIPQA \uparrow	MUSIQ \uparrow	CLIPQA \uparrow	MUSIQ \uparrow
BSRGAN [74]	1	26.51	<u>0.775</u>	<u>0.269</u>	0.5439	63.586	0.6163	63.582
Real-ESRGAN [58]	1	25.85	0.773	0.273	0.4898	59.678	0.5995	63.220
SwinIR [31]	1	26.43	0.786	0.251	0.4654	59.636	0.5782	63.822
SUPIR [71]	50	24.38	0.698	0.331	0.5449	63.676	0.6133	66.460
OSDiff [63]	1	25.25	0.737	<u>0.299</u>	0.6772	67.602	0.6836	<u>68.853</u>
ResShift [73]	15	<u>26.49</u>	0.754	0.360	0.5958	59.873	0.6537	61.330
SinSR (distill only) [59]	1	26.14	0.732	0.357	0.6119	57.118	0.6822	61.267
SinSR [59]	1	25.83	0.717	0.365	0.6887	61.582	0.7150	62.169
ResShift-VSD (Appendix A)	1	23.96	0.616	0.466	<u>0.7479</u>	63.298	0.7606	66.701
RSD (Ours , distill only)	1	24.92	0.696	0.355	0.7518	<u>66.430</u>	<u>0.7534</u>	68.383
RSD (Ours)	1	25.91	0.754	0.273	0.7060	65.860	0.7267	69.172

Table 11: Extended quantitative results of models on ImageNet-Test [73]. The best and second best results are highlighted in **bold** and underline.

Methods	NFE	PSNR \uparrow	SSIM \uparrow	LPIPS \downarrow	CLIPQA \uparrow	MUSIQ \uparrow
ESRGAN [57]	1	20.67	0.448	0.485	0.451	43.615
RealSR-JPEG [25]	1	23.11	0.591	0.326	0.537	46.981
BSRGAN [74]	1	24.42	0.659	0.259	0.581	54.697
SwinIR [31]	1	23.99	0.667	0.238	0.564	53.790
Real-ESRGAN [58]	1	24.04	0.665	0.254	0.523	52.538
DASR [33]	1	24.75	<u>0.675</u>	0.250	0.536	48.337
LDM-30 [43]	30	24.49	0.651	0.248	0.572	50.895
LDM-15 [43]	15	<u>24.89</u>	0.670	0.269	0.512	46.419
SUPIR [71]	50	22.56	0.574	0.302	0.786	<u>60.487</u>
OSDiff [63]	1	23.02	0.619	0.253	0.677	60.755
ResShift [73]	15	25.01	0.677	0.231	0.592	53.660
SinSR (distill only) [59]	1	24.69	0.664	0.222	0.607	53.316
SinSR [59]	1	24.56	0.657	0.221	0.611	53.357
ResShift-VSD (Appendix A)	1	23.69	0.624	0.230	0.665	58.630
RSD (Ours , distill only)	1	23.97	0.643	<u>0.217</u>	0.660	57.831
RSD (Ours)	1	24.31	0.657	0.193	<u>0.681</u>	58.947

Table 12: Extended quantitative results of models on crops from [56]. The best and second best results are highlighted in **bold** and underline.

Datasets	Methods	NFE	PSNR \uparrow	SSIM \uparrow	LPIPS \downarrow	DISTS \downarrow	NIQE \downarrow	MUSIQ \uparrow	MANIQA \uparrow	CLIPQA \uparrow
DIV2K-Val	BSRGAN	1	<u>24.58</u>	0.6269	0.3351	0.2275	4.7518	61.20	0.5071	0.5247
	Real-ESRGAN	1	24.29	0.6371	0.3112	0.2141	<u>4.6786</u>	61.06	0.5501	0.5277
	LDL	1	23.83	<u>0.6344</u>	0.3256	0.2227	4.8554	60.04	0.5350	0.5180
	FeMASR	1	23.06	0.5887	0.3126	0.2057	4.7410	60.83	0.5074	0.5997
	StableSR	200	23.26	0.5726	0.3113	0.2048	4.7581	65.92	0.6192	0.6771
	DiffBIR	50	23.64	0.5647	0.3524	0.2128	4.7042	65.81	0.6210	0.6704
	SeeSR	50	23.68	0.6043	0.3194	<u>0.1968</u>	4.8102	<u>68.67</u>	<u>0.6240</u>	0.6936
	PASD	20	23.14	0.5505	0.3571	0.2207	4.3617	68.95	0.6483	0.6788
	SUPIR [71]	50	22.13	0.5280	0.3923	0.2314	5.6758	63.82	0.5933	0.7147
	ResShift [73]	15	24.65	0.6181	0.3349	0.2213	6.8212	61.09	0.5454	0.6071
	SinSR [59]	1	24.41	0.6018	0.3240	0.2066	6.0159	62.82	0.5386	0.6471
	OSEDiff [63]	1	23.72	0.6108	<u>0.2941</u>	0.1976	4.7097	67.97	0.6148	0.6683
	RSD (Ours)	1	23.91	0.6042	0.2857	0.1940	5.1987	68.05	0.5937	<u>0.6967</u>
DRealSR	BSRGAN	1	28.75	0.8031	0.2883	0.2142	6.5192	57.14	0.4878	0.4915
	Real-ESRGAN	1	<u>28.64</u>	<u>0.8053</u>	<u>0.2847</u>	0.2089	6.6928	54.18	0.4907	0.4422
	LDL	1	28.21	0.8126	0.2815	<u>0.2132</u>	7.1298	53.85	0.4914	0.4310
	FeMASR	1	26.90	0.7572	0.3169	0.2235	<u>5.9073</u>	53.74	0.4420	0.5464
	StableSR	200	28.03	0.7536	0.3284	0.2269	6.5239	58.51	0.5601	0.6356
	DiffBIR	50	26.71	0.6571	0.4557	0.2748	6.3124	61.07	0.5930	0.6395
	SeeSR	50	28.17	0.7691	0.3189	0.2315	6.3967	64.93	<u>0.6042</u>	0.6804
	PASD	20	27.36	0.7073	0.3760	0.2531	5.5474	<u>64.87</u>	0.6169	0.6808
	SUPIR [71]	50	24.93	0.6360	0.4263	0.2823	7.4336	59.39	0.5537	0.6799
	ResShift [73]	15	28.46	0.7673	0.4006	0.2656	8.1249	50.60	0.4586	0.5342
	SinSR [59]	1	28.36	0.7515	0.3665	0.2485	6.9907	55.33	0.4884	0.6383
	OSEDiff [63]	1	27.92	0.7835	0.2968	0.2165	6.4902	64.65	0.5899	<u>0.6963</u>
	RSD (Ours)	1	27.40	0.7559	0.3042	0.2343	6.2577	62.03	0.5625	0.7019
RealSR	BSRGAN	1	26.39	0.7654	0.2670	<u>0.2121</u>	5.6567	63.21	0.5399	0.5001
	Real-ESRGAN	1	25.69	<u>0.7616</u>	0.2727	0.2063	5.8295	60.18	0.5487	0.4449
	LDL	1	25.28	0.7567	0.2766	<u>0.2121</u>	6.0024	60.82	0.5485	0.4477
	FeMASR	1	25.07	0.7358	0.2942	0.2288	5.7885	58.95	0.4865	0.5270
	StableSR	200	24.70	0.7085	0.3018	0.2288	5.9122	65.78	0.6221	0.6178
	DiffBIR	50	24.75	0.6567	0.3636	0.231	5.5346	64.98	0.6246	0.6463
	SeeSR	50	25.18	0.7216	0.3009	0.2223	5.4081	69.77	<u>0.6442</u>	0.6612
	PASD	20	25.21	0.6798	0.3380	0.2260	<u>5.4137</u>	68.75	0.6487	0.6620
	SUPIR [71]	50	23.61	0.6606	0.3589	0.2492	5.8877	63.21	0.5895	<u>0.6709</u>
	ResShift [73]	15	<u>26.31</u>	0.7421	0.3421	0.2498	7.2365	58.43	0.5285	0.5442
	SinSR [59]	1	26.28	0.7347	0.3188	0.2353	6.2872	60.80	0.5385	0.6122
	OSEDiff [63]	1	25.15	0.7341	0.2921	0.2128	5.6476	<u>69.09</u>	0.6326	0.6693
	RSD (Ours)	1	25.61	0.7420	<u>0.2675</u>	0.2205	5.7500	66.02	0.5930	0.6793

E Details of ResShift

As a part of the diffusion model class, ResShift can be described by specifying the forward (degradation) process, the parametrization of the reverse (restoration) process, and the objective for training the reverse process.

Forward process. Consider a pair of (LR, HR) images $(y_0, x_0) \sim p_{\text{data}}(y_0, x_0)$. For a residual $e_0 = y_0 - x_0$, ResShift proposes to transit from x_0 to y_0 with the Markov chain $\{x_t\}_{t=1}^T$ of length T through the following Gaussian transition distribution:

$$q(x_t|x_{t-1}, y_0) = \mathcal{N}(x_t|x_{t-1} + \alpha_t e_0, \kappa^2 \alpha_t \mathbf{I}), \quad (20)$$

where:

- $\alpha_t = \eta_t - \eta_{t-1}$ for $t > 1$ and $\alpha_1 = \eta_1$ are defined by the shifting sequence $\{\eta_t\}_{t=1}^T$, \mathbf{I} denotes the identity matrix.
- κ is a hyper-parameter controlling the noise variance and the shifting sequence $\{\eta_t\}_{t=1}^T$ monotonically increases with the timestep t .

The transition distribution (1) leads to analytically tractable marginal distribution of $q(x_t|x_0, y_0)$ at any timestep t :

$$q(x_t|x_0, y_0) = \mathcal{N}(x_t|x_0 + \eta_t e_0, \kappa^2 \eta_t \mathbf{I}), t \in [1, T], \quad (21)$$

The shifting sequence satisfies $\eta_1 \approx 0$ and $\eta_T \approx 1$, which guarantee the convergence of marginal distributions of x_1 and x_T to approximate distributions of the HR image and the LR image respectively. Notably, the posterior distribution $q(x_{t-1}|x_t, x_0, y_0)$ for the transition distribution (1) is tractable and can be derived using the Bayes's rule:

$$q(x_{t-1}|x_t, x_0, y_0) = \mathcal{N}\left(x_{t-1} \middle| \frac{\eta_{t-1}}{\eta_t} x_t + \frac{\alpha_t}{\eta_t} x_0, \kappa^2 \frac{\eta_{t-1}}{\eta_t} \alpha_t \mathbf{I}\right). \quad (22)$$

Reverse process. ResShift suggests the construction of the reverse process to estimate the posterior distribution $p(x_0|y_0)$ in the following parametrized form:

$$p_\theta(x_0|y_0) = \int p(x_T|y_0) \prod_{t=1}^T p_\theta(x_{t-1}|x_t, y_0) dx_{1:T} \quad (23)$$

Here $p(x_T|y_0) \approx \mathcal{N}(x_T|y_0, \kappa^2 \mathbf{I})$ and $p_\theta(x_{t-1}|x_t, y_0)$ is the inverse transition kernel from x_{t-1} to x_t with learnable parameters θ . Following DDPM [20], ResShift parametrizes this transition kernel with the Gaussian:

$$p_\theta(x_{t-1}|x_t, y_0) = \mathcal{N}(x_{t-1}|\mu_\theta(x_t, y_0, t), \Sigma_\theta(x_t, y_0, t)) \quad (24)$$

Objective. To derive the minimization objective for parameters θ , ResShift applies the variational bound estimation on negative log-likelihood for the $p_\theta(x_0|y_0)$, as in DDPM:

$$\min_{\theta} \mathbb{E}_{(x_0, y_0)} \sum_{t=1}^T \mathbb{E}_{x_t \sim q(x_t|x_0, y_0)} [\mathcal{D}_{KL}(q(x_{t-1}|x_t, x_0, y_0) || p_\theta(x_{t-1}|x_t, y_0))] \quad (25)$$

Inspired by the tractable formula for the posterior $q(x_{t-1}|x_t, x_0, y_0)$ in (22), ResShift sets the variance parameter $\Sigma_\theta(x_t, y_0, t)$ to be independent of x_t and y_0 and reparametrized the parameter $\mu_\theta(x_t, y_0, t)$ as follows:

$$\Sigma_\theta(x_t, y_0, t) = \kappa^2 \frac{\eta_{t-1}}{\eta_t} \alpha_t \mathbf{I} \quad (26)$$

$$\mu_\theta(x_t, y_0, t) = \frac{\eta_{t-1}}{\eta_t} x_t + \frac{\alpha_t}{\eta_t} f_\theta(x_t, y_0, t), \quad (27)$$

where f_θ is a deep neural network with parameter θ , aiming to predict x_0 . Given the Gaussian form of the distributions $q(x_{t-1}|x_t, x_0, y_0)$ (22) and $p_\theta(x_{t-1}|x_t, y_0)$ (24), the objective (25) simplifies as follows:

$$\min_{\theta} \left[\sum_{t=1}^T w_t \mathbb{E}_{(x_0, y_0, x_t)} \|f_\theta(x_t, y_0, t) - x_0\|^2 \right], \quad (28)$$

where $w_t = \frac{\alpha_t}{2\kappa^2 \eta_t \eta_{t-1}}$. Empirically, the omitting the weight w_t leads to a noticeable improvement in performance, which aligns with the conclusion in DDPM.

F Limitations, failure cases, potential societal impact

Limitations and failure cases. Below, we present failure cases for image restoration for RSD and baselines. Our method may produce images with mistakes since the teacher model is imperfect. However, we stress that T2I-based SR models with rich priors also have such problems. Specifically, in Figure 5 (top), we observe that the teacher model produces an indistinguishable image from the simple bicubic upsampling image. A similar occurs with OSedDiff, while all other methods, including ours, SinSR, SUPIR, and GAN-based models, produce images with visible artifacts. The other typical failure case of diffusion-based methods, ResShift, SinSR, and RSD, includes images with rich background details, which are hard to predict given insufficient contextual information on the LR image. As we show in Figure 5 (bottom), hallucination properties of T2I-based methods, SUPIR and OSedDiff, provide realistic continuation of the road and cars with greater and richer details compared to results of ResShift, SinSR, and RSD. In Figure 6, we show failure cases of considered SR methods on the real-world RealSR benchmark [3] with available ground truth images. All methods struggle when running on images with many small details, like computer details and bush patterns. Hallucinations of diffusion-based methods don’t coincide with the original HR image in small details. Figure 7 demonstrates several failure cases for real-world SR methods on synthetic low-resolution crops of StableSR [56], which were obtained from DIV2K dataset [1] using Real-ESRGAN degradations [58]. Due to the lack of context diffusion-based methods, ResShift, SinSR, and RSD failed to reconstruct details of the squirrel’s body and forest, as well as T2I-based SUPIR and OSedDiff methods with richer prior. Their predictions have significant visual differences with ground truth HR images.

Potential societal impact. Our proposed distillation method of the diffusion-based image super-resolution model, RSD, presents potential positive and negative societal impacts. On the positive side, the practical effect of the techniques developed to improve the quality and efficiency of the real-world SR model ranges from improving medical imaging for diagnostic purposes and assisting in disaster response to improving remote sensing and autonomous driving performance. However, there are concerns regarding the generation of fake content. Our model is generative and can generate deepfakes for disinformation. But we note that our model was trained using only one dataset, ImageNet [9], which is known to be standard in SR research [18, 59, 73]. Thus, we don’t expect any high risk for misuse of the trained model as long as the training data does not contain unsafe images.

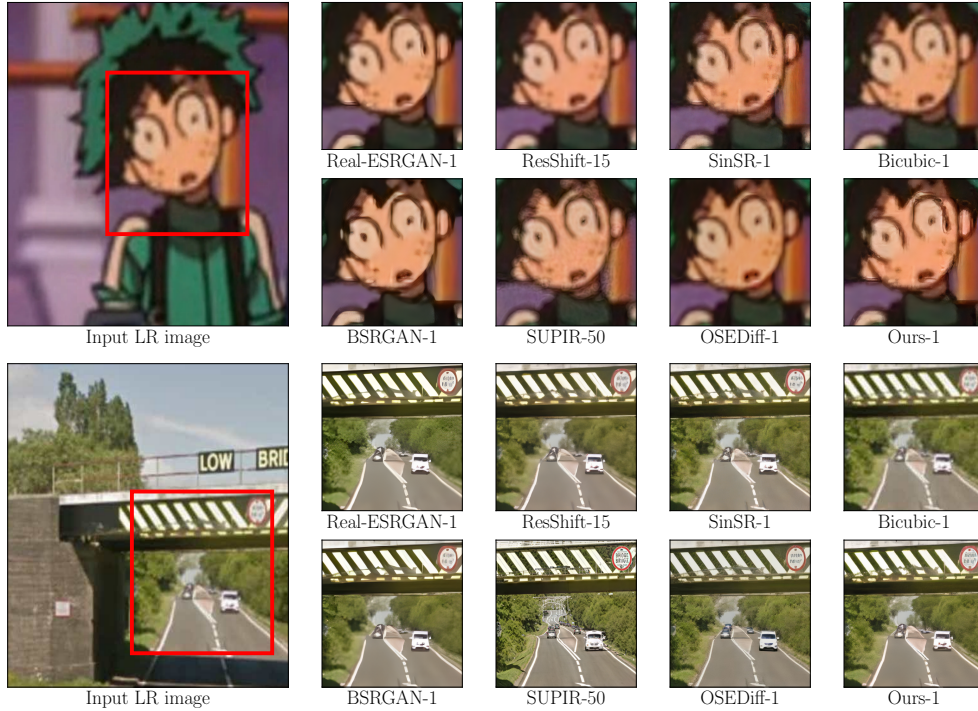


Figure 5: Failure cases on images from RealSet65 [73]. Please zoom in for a better view.



Figure 6: Failure cases on images from RealSR [73]. Please zoom in for a better view.

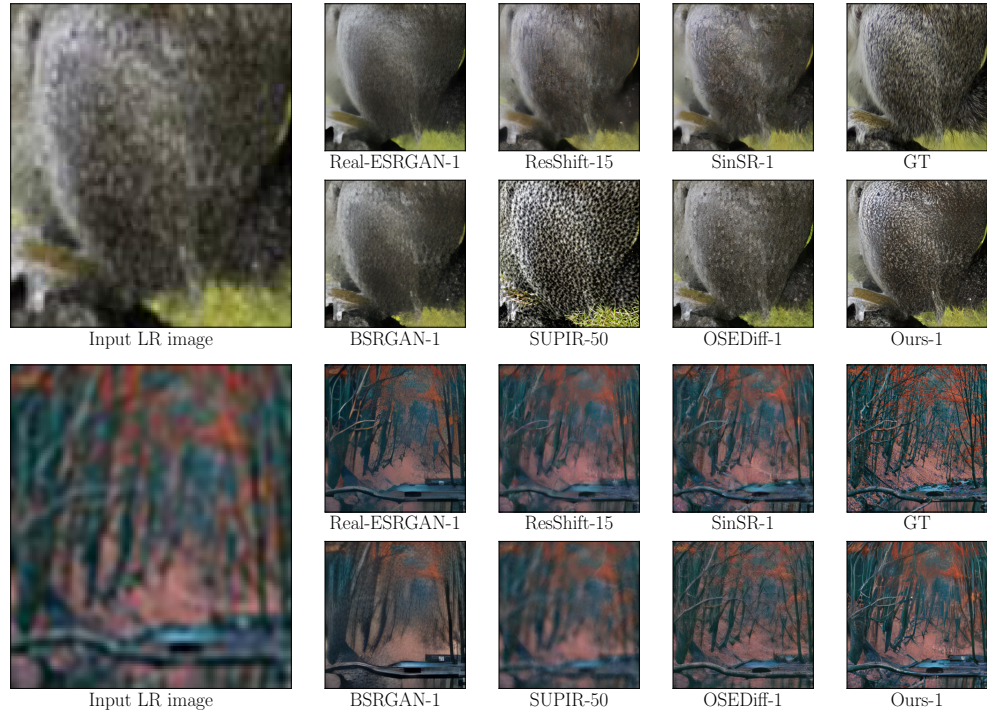


Figure 7: Failure cases on synthetic images from DIV2K crops [1, 56]. Please zoom in for a better view.

G Proofs

Proof of Proposition 3.1. First stage. We first prove that using objective $\mathcal{L}_{\text{fake}}$ (see Eq. (7)) is equivalent to training a fake model f_ϕ with objective (5). We recall the $\mathcal{L}_{\text{fake}}$ minimization objective:

$$\arg \min_{\phi} \mathcal{L}_{\text{fake}}, \quad (29)$$

where

$$\mathcal{L}_{\text{fake}} = \left(\sum_{t=1}^T w_t \mathbb{E}_{p_\theta(\hat{x}_0, y_0, x_t)} \left\{ \|f_\phi(x_t, y_0, t)\|_2^2 - 2\langle f_\phi(x_t, y_0, t) + \underbrace{f^*(x_t, y_0, t)}_{\text{Does not depend on } \phi}, \hat{x}_0 \rangle \right\} \right) \quad (30)$$

Then we prove:

$$\begin{aligned} & \arg \min_{\phi} \underbrace{\left(\sum_{t=1}^T w_t \mathbb{E}_{p_\theta(\hat{x}_0, y_0, x_t)} \|f_\phi(x_t, y_0, t) - \hat{x}_0\|_2^2 \right)}_{\text{Training a fake model } f_\phi \text{ with objective (5)}} = \\ & \arg \min_{\phi} \left(\sum_{t=1}^T w_t \mathbb{E}_{p_\theta(\hat{x}_0, y_0, x_t)} \left\{ \|f_\phi(x_t, y_0, t)\|_2^2 - 2\langle f_\phi(x_t, y_0, t), \hat{x}_0 \rangle \right\} + \right. \\ & \quad \left. \underbrace{\sum_{t=1}^T w_t \mathbb{E}_{p_\theta(\hat{x}_0, y_0, x_t)} \|\hat{x}_0\|_2^2}_{\text{Does not depend on } \phi} \right) = \\ & \arg \min_{\phi} \left(\sum_{t=1}^T w_t \mathbb{E}_{p_\theta(\hat{x}_0, y_0, x_t)} \left\{ \|f_\phi(x_t, y_0, t)\|_2^2 - 2\langle f_\phi(x_t, y_0, t), \hat{x}_0 \rangle \right\} \right) = \\ & \arg \min_{\phi} \left(\sum_{t=1}^T w_t \mathbb{E}_{p_\theta(\hat{x}_0, y_0, x_t)} \left\{ \|f_\phi(x_t, y_0, t)\|_2^2 - 2\langle f_\phi(x_t, y_0, t), \hat{x}_0 \rangle \right\} - \right. \\ & \quad \left. \underbrace{\sum_{t=1}^T w_t \mathbb{E}_{p_\theta(\hat{x}_0, y_0, x_t)} \left\{ 2\langle f^*(x_t, y_0, t), x_0 \rangle \right\}}_{\text{Does not depend on } \phi} \right) = \\ & \arg \min_{\phi} \left(\sum_{t=1}^T w_t \mathbb{E}_{p_\theta(\hat{x}_0, y_0, x_t)} \left\{ \|f_\phi(x_t, y_0, t)\|_2^2 - \right. \right. \\ & \quad \left. \left. 2\langle f_\phi(x_t, y_0, t) + \underbrace{f^*(x_t, y_0, t)}_{\text{Does not depend on } \phi}, \hat{x}_0 \rangle \right\} \right) = \\ & \arg \min_{\phi} \mathcal{L}_{\text{fake}}. \quad (31) \end{aligned}$$

Second stage. Now we prove that:

$$\begin{aligned} & \underbrace{\sum_{t=1}^T w_t \mathbb{E}_{p_\theta(\hat{x}_0, y_0, x_t)} \|f_{G_\theta}(x_t, y_0, t) - f^*(x_t, y_0, t)\|_2^2}_{\mathcal{L}_\theta} = \\ & - \min_{\phi} \left\{ \sum_{t=1}^T w_t \mathbb{E}_{p_\theta(\hat{x}_0, y_0, x_t)} \left(\|f_\phi(x_t, y_0, t)\|_2^2 - \|f^*(x_t, y_0, t)\|_2^2 + \right. \right. \\ & \quad \left. \left. 2\langle f^*(x_t, y_0, t) - f_\phi(x_t, y_0, t), \hat{x}_0 \rangle \right) \right\} \quad (32) \end{aligned}$$

Note, that since ResShift objective (28) is an MSE, the solution f_{G_θ} for the data produced by generator G_θ is given by the conditional expectation as:

$$f_{G_\theta}(x_t, y_0, t) = \mathbb{E}_{p_\theta(\hat{x}_0 | y_0, x_t)}[\hat{x}_0]. \quad (33)$$

We start from the right part of (32) and transform it back to the left part:

$$\begin{aligned}
& - \min_{\phi} \left\{ \sum_{t=1}^T w_t \mathbb{E}_{p_{\theta}(\hat{x}_0, y_0, x_t)} \left(- \|f^*(x_t, y_0, t)\|_2^2 + \|f_{\phi}(x_t, y_0, t)\|_2^2 + \right. \right. \\
& \qquad \qquad \qquad \left. \left. 2 \langle f^*(x_t, y_0, t) - f_{\phi}(x_t, y_0, t), \hat{x}_0 \rangle \right) \right\} = \\
& \qquad \sum_{t=1}^T w_t \mathbb{E}_{p_{\theta}(\hat{x}_0, y_0, x_t)} \left\{ \|f^*(x_t, y_0, t)\|_2^2 - 2 \langle f^*(x_t, y_0, t), \hat{x}_0 \rangle \right\} - \\
& \min_{\phi} \left\{ \sum_{t=1}^T w_t \mathbb{E}_{p_{\theta}(\hat{x}_0, y_0, x_t)} \left(\|f_{\phi}(x_t, y_0, t)\|_2^2 - 2 \langle f_{\phi}(x_t, y_0, t), \hat{x}_0 \rangle \right) \right\} = \\
& \sum_{t=1}^T w_t \mathbb{E}_{p_{\theta}(y_0, x_t)} \left(\|f^*(x_t, y_0, t)\|_2^2 - 2 \langle f^*(x_t, y_0, t), \underbrace{\mathbb{E}_{p_{\theta}(\hat{x}_0 | y_0, x_t)} \hat{x}_0}_{f_{G_{\theta}}(x_t, y_0, t)} \rangle \right) - \\
& \min_{\phi} \left\{ \sum_{t=1}^T w_t \mathbb{E}_{p_{\theta}(\hat{x}_0, y_0, x_t)} \left(\|f_{\phi}(x_t, y_0, t)\|_2^2 - 2 \langle f_{\phi}(x_t, y_0, t), \hat{x}_0 \rangle \right) \right\} = \\
& \sum_{t=1}^T w_t \mathbb{E}_{p_{\theta}(y_0, x_t)} \left(\|f^*(x_t, y_0, t)\|_2^2 - 2 \langle f^*(x_t, y_0, t), f_{G_{\theta}}(x_t, y_0, t) \rangle \right) - \\
& \sum_{t=1}^T w_t \mathbb{E}_{p_{\theta}(y_0, x_t)} \left(\|f_{G_{\theta}}(x_t, y_0, t)\|_2^2 - 2 \underbrace{\langle f_{G_{\theta}}(x_t, y_0, t), f_{G_{\theta}}(x_t, y_0, t) \rangle}_{\|f_{G_{\theta}}\|_2^2} \right) = \\
& \sum_{t=1}^T w_t \mathbb{E}_{p_{\theta}(y_0, x_t)} \left(\|f^*(x_t, y_0, t)\|_2^2 - 2 \langle f^*(x_t, y_0, t), f_{G_{\theta}}(x_t, y_0, t) \rangle + \|f_{G_{\theta}}(x_t, y_0, t)\|_2^2 \right) = \\
& \qquad \qquad \qquad \sum_{t=1}^T w_t \mathbb{E}_{p_{\theta}(y_0, x_t)} \underbrace{\|f_{G_{\theta}}(x_t, y_0, t) - f^*(x_t, y_0, t)\|_2^2}_{\text{Does not depend on } \hat{x}_0 \text{ so we can add } \hat{x}_0 \text{ in expectation.}} = \\
& \qquad \qquad \qquad \sum_{t=1}^T w_t \mathbb{E}_{p_{\theta}(\hat{x}_0, y_0, x_t)} \|f_{G_{\theta}}(x_t, y_0, t) - f^*(x_t, y_0, t)\|_2^2.
\end{aligned}$$

□

H More visual results

This section provides an additional qualitative visual comparisons between RSD and other baselines on two real-world full-size and two synthetic benchmarks with available ground truth data.

1. Full-size benchmark RealSR [3]. The results are shown in Figure 8.
2. Full-size benchmark DRealSR [62]. The results are shown in Figure 9.
3. Synthetic benchmark ImageNet-Test [9, 73]. The results are shown in Figure 10.
4. Synthetic benchmark DIV2K [1, 56]. The results are shown in Figure 11.

The baseline methods include multistep diffusion-based SR methods (ResShift [73], SUPIR [71]), 1-step diffusion-based SR methods (SinSR [59], OSEDiff [63]), and GAN-based SR methods (RealESRGAN [58] and BSRGAN [74]).

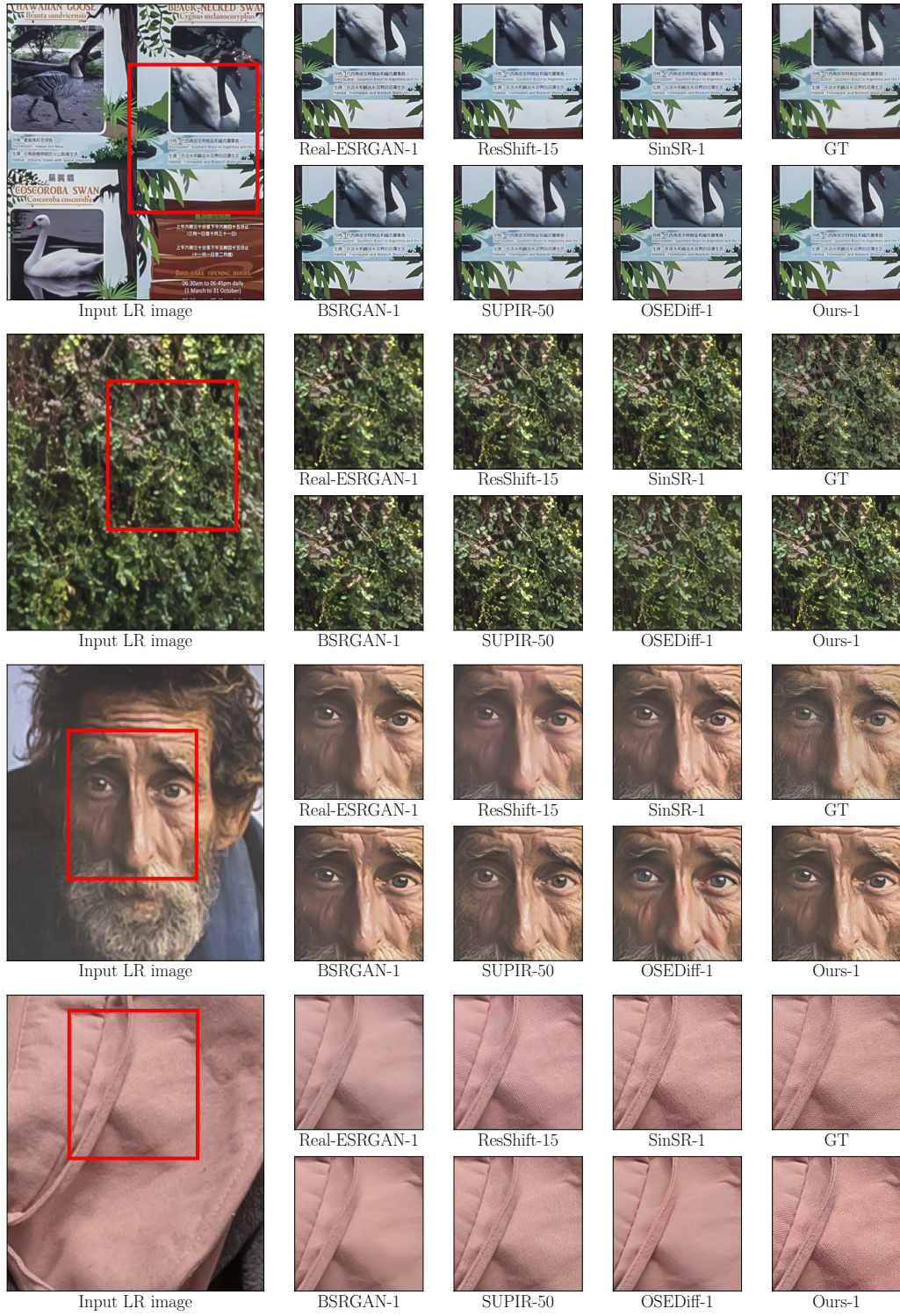


Figure 8: Visual comparison on real-world samples from RealSR [3]. Please zoom in for a better view.

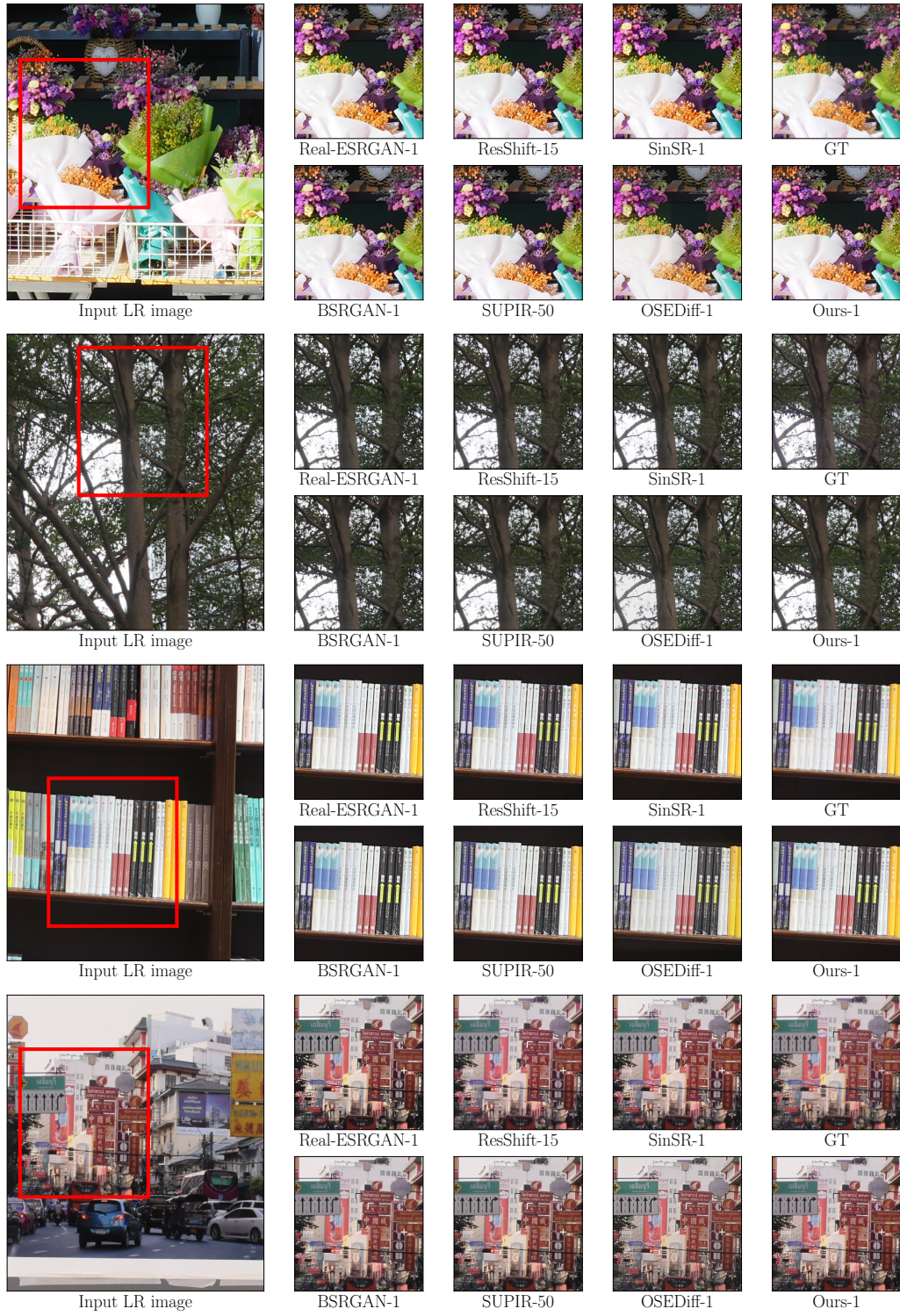


Figure 9: Visual comparison on real-world samples from DRealSR [62]. Please zoom in for a better view.

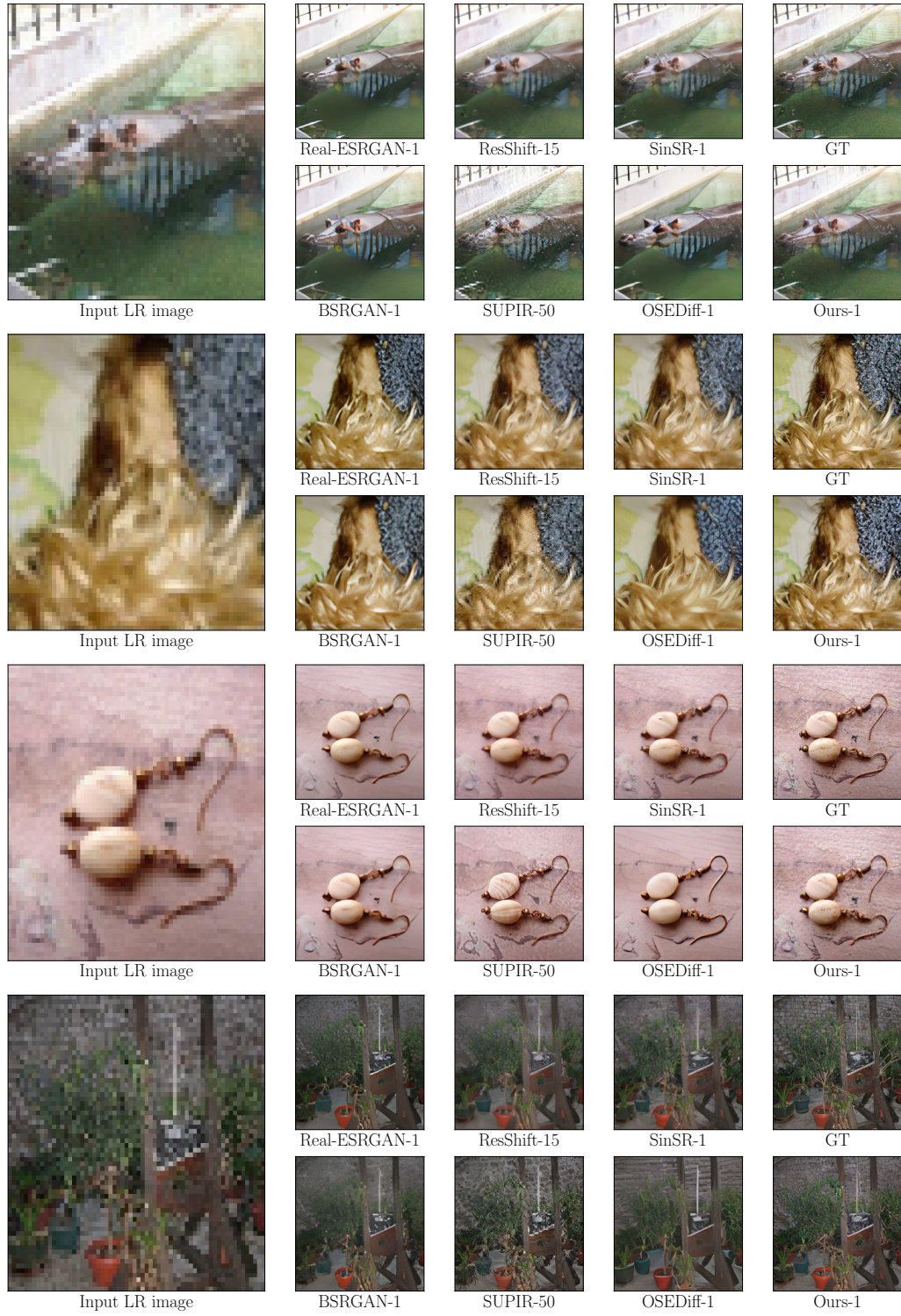


Figure 10: Visual comparison on synthetic samples from ImageNet-Test [9, 73]. Please zoom in for a better view.

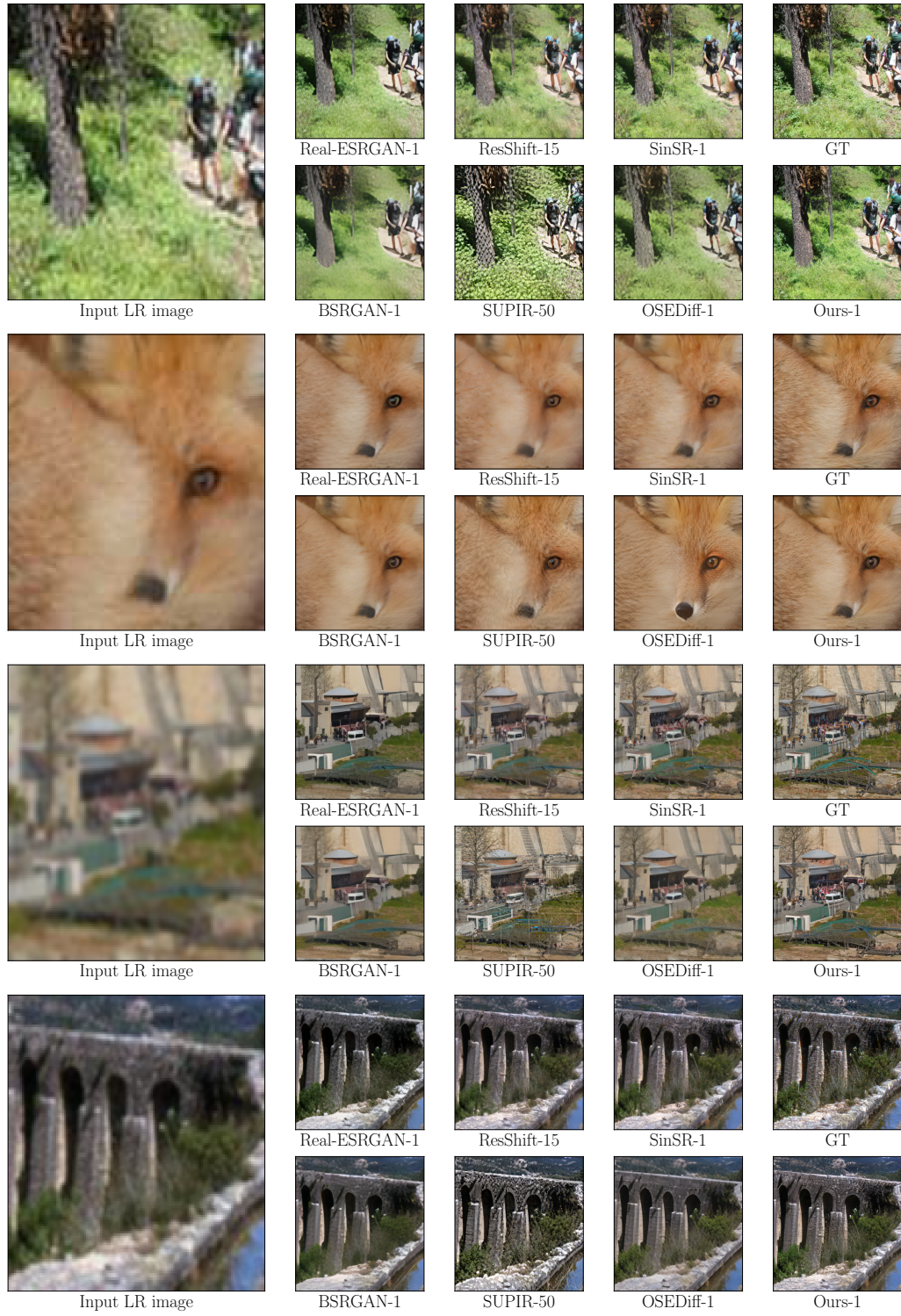


Figure 11: Visual comparison on synthetic samples from DIV2K crops [1, 56]. Please zoom in for a better view.